Mohammad R. Hossan[1]
Diganta Dutta[2]
Nazmul Islam[3]
Prashanta Dutta[4]

[1]Department of Engineering and Physics, University of Central Oklahoma, Edmond, OK, USA
[2]Department of Physics, University of Nebraska, Kearney, NE, USA
[3]Department of Electrical Engineering, University of Texas Rio Grande Valley, TX, USA
[4]School of Mechanical and Materials Engineering, Washington State University, Pullman, WA, USA

Received September 25, 2017
Revised October 31, 2017
Accepted November 1, 2017

Review

Review: Electric field driven pumping in microfluidic device

Pumping of fluids with precise control is one of the key components in a microfluidic device. The electric field has been used as one of the most popular and efficient nonmechanical pumping mechanism to transport fluids in microchannels from the very early stage of microfluidic technology development. This review presents fundamental physics and theories of the different microscale phenomena that arise due to the application of an electric field in fluids, which can be applied for pumping of fluids in microdevices. Specific mechanisms considered in this report are electroosmosis, AC electroosmosis, AC electrothermal, induced charge electroosmosis, traveling wave dielectrophoresis, and liquid dielectrophoresis. Each phenomenon is discussed systematically with theoretical rigor and role of relevant key parameters are identified for pumping in microdevices. We specifically discussed the electric field driven body force term for each phenomenon using generalized Maxwell stress tensor as well as simplified effective dipole moment based method. Both experimental and theoretical works by several researchers are highlighted in this article for each electric field driven pumping mechanism. The detailed understanding of these phenomena and relevant key parameters are critical for better utilization, modulation, and selection of appropriate phenomenon for efficient pumping in a specific microfluidic application.

Keywords:
Dielectrophoresis / Electroosmosis / Electrothermal / Lab-on-a-chip / Micropump
DOI 10.1002/elps.201700375

1 Introduction

In last two decades, there are significant interests in the microfluidic-based separation platforms because these devices can provide rapid separation with higher resolution and whole channel detection, require smaller sample volume and consume much less reagent, are cheap to fabricate and disposable, need lower electric potential, etc. [1–6]. To perform the complete analysis in these lab-on-a-chip microfluidic devices, several functionalities have to be integrated. One of the key functionalities of these devices is pumping, which is needed for transporting the separated bands, moving reagents to the separation/mixing chamber, supplying the ligands/antibodies to the binding sites, etc. Since most microfluidic-based separations are performed applying an electric field, it is desirable to have an electric field driven nonmechanical pumping system. The key focus of this work is to highlight the recent progress made in the electric field driven pumping mechanisms of liquids in microfluidic chips.

Correspondence: Dr. Prashanta Dutta, Professor of Mechanical Engineering, Washington State University, Pullman, WA 99164-2920, USA
E-mail: prashanta@wsu.edu

Abbreviations: ACET, AC electrothermal technique; **ACEO**, AC electroosmosis; **EDL**, electric double layer; **ICEO**, induced charge electroosmosis; **LDEP**, liquid dielectrophoresis; **MST**, Maxwell Stress Tensor; **twDEP**, traveling wave dielectrophoresis

When an electric field is applied to a liquid in a microfluidic device, a number of phenomena might occur depending on the type of liquids, liquid-surface interface, and nature of electric fields, which are generally known as electrokinetics. Although the first electrokinetic phenomenon is observed more than two-century back, many of them have only started getting attention in the late 1980s with the advent of the miniaturization techniques needed for this type of microdevice [7].

The major electrokinetic phenomena observed in microdevices are electroosmosis, electrophoresis, dielectrophoresis, Joule heating related electrothermal effect, induced charge electroosmosis, etc. Both electroosmosis and electrophoresis have century-long history and they are very widely explored in the context of separation. Electrophoresis is the motion of the charged particles or macromolecules in an electrolyte solution under the action of an applied electric field. The primary application of electrophoresis is to separate one analyte from others or to concentrate a species from a dilute solution for detection or further processing. Depending on the type of electrolytes used, electrophoresis can be sub-divided into zone electrophoresis, moving boundary electrophoresis, isotachophoresis, isoelectric focusing, etc. [8]. These electrophoretic techniques are the workhorses of most analytical and bioanalytical works. To improve the separation resolution, two or more electrophoretic techniques

Color Online: See the article online to view Figs. 1–6, 11, 14–20 and 22 in color.

can be hyphenated. In some instances, electrophoretic techniques are integrated with other types of separation methods, such as mass spectrometry to develop 2D or 3D separation platforms [1, 9, 10].

Electroosmosis is the motion of ionized liquid with respect to a stationary charged or polarized surfaces in presence of an applied electric field [11]. It is one of the very popular pumping technique used in the microfluidic device. Depending on the nature of the applied electric field and device configuration, electroosmosis can be classified as DC electroosmosis, time-periodic electroosmosis, AC electroosmosis and induced charge electroosmosis.

The history of DC electroosmosis goes back to 1809 when Reuss demonstrated the motion of fluid from the anode to cathode in a porous clay diaphragms [12]. In the mid 19th century, Wiedemann repeated the experiment and described the fundamentals of this phenomenon [13]. Until the early 1990s, most of the DC electroosmosis was restricted in capillary tubes, though the fundamental analysis for pure electroosmotic flow has been reported for both rectangular [14] and circular channels [15]. In 2002, a group of researchers has quantified the electroosmotic flow velocity distribution in a rectangular microchannel using microparticle image velocimetry, where they have demonstrated the plug like velocity distribution [16].

The time periodic electroosmosis concept was introduced by Dutta and Beskok in 2001 by applying an AC electric field along the channel [17]. In time periodic electroosmotic flow, the general structure of electric double layer remains the same, but the flow switches direction due to the change in the electric field direction. Later, these phenomena were extended to various microchannel geometries [18–20] and non-Newtonian fluids [21–23]. Although this technique has some merits for mixing of species in microchannels [24], it cannot be applied for pumping of fluids.

Unlike DC or time-periodic electroosmosis, in ACEO (AC electroosmosis), the surface charges are induced by externally applied voltages through the embedded electrode rather than from the naturally occurring charges on the channel surfaces [25]. Thus, the charge build-ups are hundreds of times stronger than DC electroosmosis. As a result, this technique can generate locally stronger forcing field for fluid flow. However, the ACEO technique is much more intricate as one must design and fabricate electrodes on the microchannel surface using expensive fabrication techniques. Also, unlike DC electroosmosis, this method cannot be used for pressure build-ups, but an appropriately designed ACEO platform can provide local control in fluid flow which might be useful in many lab-on-a-chip devices.

Similar to ACEO, AC electrothermal (ACET) technique can be used for pumping of conductive fluids using an AC electric field through embedded electrodes on the channel surface [26]. Unlike ACEO, the ACET is operated at a higher frequency to avoid bubble formation due to the Faradic reaction. In ACET, the electric double layer cannot be formed next to the electrodes as the electrodes are energized at a frequency higher than the charge relaxation frequency.

The electric field can also be applied to transport micron and submicron sized particles immersed in a fluid. If these particles are charged, their motion is governed by the electrophoresis or combined electrophoresis and electroosmosis. On the other hand, if these particles are neutral (uncharged), it is still possible to manipulate them using a technique called dielectrophoresis [27]. Like ACEO and ACET, dielectrophoresis requires a non-uniform electric field to move particles. In dielectrophoresis, an electric field is applied to the particles through a liquid or electrolyte. The applied electric field serves two purposes: it polarizes the particles and moves the particles towards the appropriate electric field zone. For instance, if the particle is more (less) polarizable than the media, it moves towards the higher (lower) electric field regions, which is known as positive (negative) dielectrophoresis. By introducing appropriate phase lags between consecutive electrodes [28, 29], it is possible to move particles in a preferred direction, which can introduce a fluid motion due to the viscous interaction between the particles and fluid. This phenomenon is popularly known as traveling wave dielectrophoresis (twDEP).

Another interesting electric field driven pumping mechanism is induced charge electroosmosis (ICEO) [30]. This technique shares some traits from both electroosmosis and dielectrophoresis. In induced charge electroosmosis, a stationary neutral post or charged surface can be polarized, one side has one type of net charge and the other side has the opposite net charge, using an electric field. The net surface charge (developed on the particle) from the polarization process can generate oppositely charged EDLs on the two sides of the particles, and the interaction of EDL and electric field can generate flow.

From aforementioned discussion, it is clear that not all electrokinetic phenomena are used for microfluidic pumping. In this review, we focus on a few major electrokinetic phenomena that have been reported as a potential pumping mechanism, either globally or locally, in the literature. The rest of the paper is organized as follows: First, we present the general governing equations for both linear and nonlinear electrokinetic phenomena. Next, we briefly introduce the working principles of various electric field driven pumping mechanisms. This is followed by the specific and simplified governing equations as well as auxiliary conditions for each pumping mechanisms. Then, we only review important works in this area. It is important to note that there are thousands of publications on electrokinetic pumping, and it is impossible to review all of them. In this review, our primary focus was to delineate the fundamental working principles of each electric field driven pumping technique along with similarities and dissimilarities among them. Readers are advised to consult the individual review papers on each topic for further information.

2 Background

Electrokinetics is a result of complex interaction among fluid species, electric field, induced thermal energy, dissolved ions,

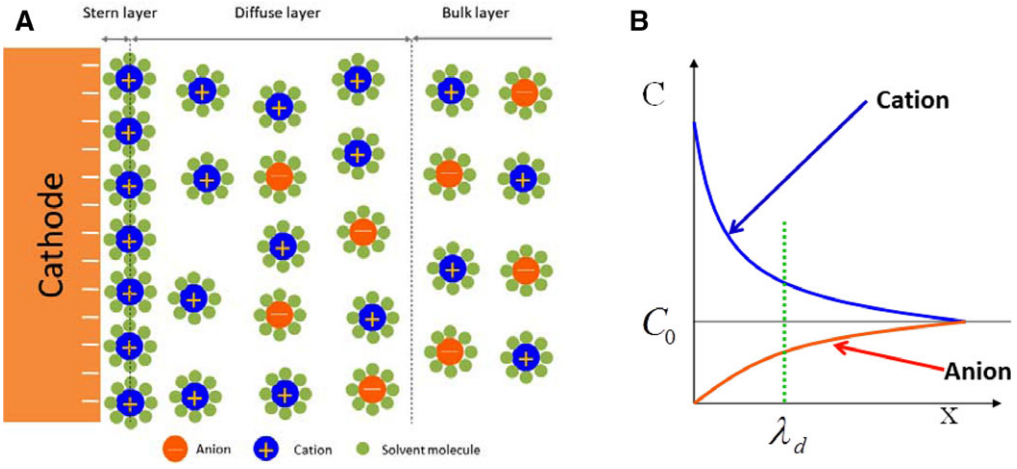

Figure 1. (A) Formation of an electric double layer next to a negatively charged surface. The Stern layer is also known as compact layer and it consists of inner and outer Helmholtz layer (not shown). The electrostatic action is very dominant in the Stern/compact layer. The diffuse layer is impacted by the Coulombic interaction and random thermal motion. (B) The qualitative plot of co-ion (anions) and counterions (cations) distribution in an electric double layer. The electrolyte is electroneutral in the bulk regime, where the concentrations of cations and anions are same.

and object polarization. These interactions are governed by a number of equations which are discussed below. Depending on the types of electrokinetic phenomenon, one or more interactions play a dominant role, while other interactions can be safely ignored.

2.1 Formation of an electric double layer

Electric double layer (EDL) forms when a charged surface comes in contact with an electrolyte, a liquid with free or mobile ions. Due to the presence of charges on the surface, the ions get redistributed close to the surface as shown in Fig. 1A. The formation of EDL next to a charged surface is the primary factor responsible for different types of electroosmosis.

In a dilute solution, the electric double layer consists of Stern and diffuse layers. The Stern layer is generally formed by an immobilized layer of counter ions (positive ions in this case) from the electrolyte, where the electrostatic interaction is very dominant. In the diffuse layer, both electrostatic and thermal energy play key roles. The concentration of the counter ions decreases from the charged surface, while the concentration of co-ions increases as shown in Fig. 1B. At some distance from the charged surface, the electrostatic energy is balanced by the thermal energy, and that length scale is known as Debye length. For a symmetric binary electrolyte, the Debye length can be expressed as [31]

$$\lambda_D = \sqrt{\frac{\varepsilon k_B T}{2z^2 e^2 C_o}} \tag{1}$$

where ε is the permittivity of the fluid medium, k_B is the Boltzmann constant, T is the temperature in absolute form, e is the electron charge, z is the valence, and C_0 is the concentration of ions in the bulk or electroneutral region. This relationship suggests that Debye length strongly depends on the electrolyte concentration, and it will be larger for a dilute solution compared to a concentrated one. Generally, the Debye length varies between 0.1 to 10 nm, which is much smaller than the typical microfluidic channel dimension (height or width), but for nanochannel, it is comparable to the channel dimension.

2.2 Electric double layer for nonlinear electrokinetics

In many microfluidic applications, such as AC electroosmosis, electrothermal, etc., a large electric field is applied to electrodes patterned on the channel surface. For the large charge density or large applied potential drop across the electric double layer, the inner diffuse layer is overcrowded [32], which is termed as condensed layer as shown in Fig. 2. Like the low surface potential case, both Stern layer and outer diffuse layers are present in this scenario.

When applied electric potential (ψ) is much larger than the thermal potential ($\psi_T = k_B T/ez$), the dilute solution theory breaks down. This breakdown is not due to the exponential counter-ion distribution, but due to the Steric effects. The Steric limit is reached at the maximum concentration, and the corresponding critical potential [32].

$$\psi_c = \frac{k_B T}{ez} \ln\left(\frac{C_{\max}}{C_0}\right) \tag{2}$$

At steric limit, the maximum concentration of counter ions can be given as

$$C_{\max} = \frac{1}{a^3} \tag{3}$$

where a is the typical spacing between densely packed ions considering hydration effects and ion-ion interactions. In a series of papers [32], Bazant and co-workers have presented the dynamics of electrolytes at large applied electric

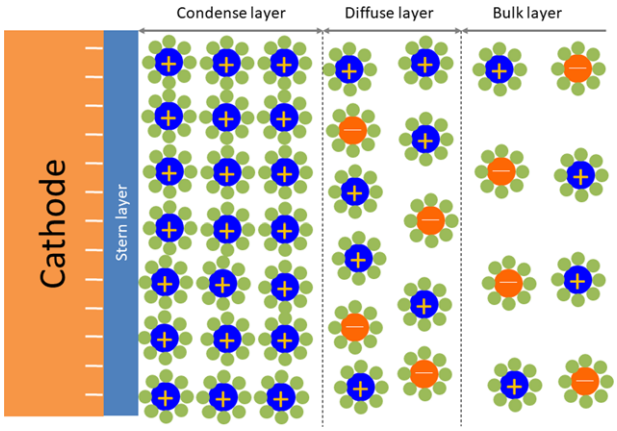

Figure 2. Formation of an electric double layer for large applied potential ($\psi_s >> k_B T/e$) on the surface or large surface charge density. Essential layers in the fluid domain (from left to right) are Stern, condensed (inner diffuse) and outer diffuse layer. In this specific case, the inner diffuse layer consists of more than one layer of counter-ions forming a condensed layer. Due to the overcharging of the double layer, the dilute solution theory described in classical (DC) electroosmosis is not valid here. Adopted from Kilic et al. [32].

potential, and they have identified linear, weakly linear and highly nonlinear regimes as

Linear: $\psi < \psi_T$

Weakly nonlinear: $\psi_T < \psi < \psi_c$

Highly nonlinear: $\psi > \psi_c$

The steric effect will be dominant in many nonlinear electrokinetic phenomena, such ACEO and ACET. Thus, readers are advised to consult the earlier works of Bazant and co-workers [32] on steric effects for AC electrokinetic processes where energizing electrodes are placed on the channel walls.

2.3 Polarization of an object

Polarization is a process of accumulation of positive and negative charges at the two sides of the object or at the two sides of the interface between objects and fluid as shown in Fig 3. The accumulation of charges on the object also induces polarization within the fluid (Fig. 3B). The result of this is the formation of dipolar charge double layer, which facilitates different electrokinetic phenomena. For instance, if the applied electric field is spatially nonuniform, it creates a net force on the object and causes motion of the object in the fluid medium, which is known as dielectrophoresis (DEP). On the other hand, for a fixed post or an object, the dipolar charge double layer can facilitate fluid flow, and this phenomenon is termed as induced charge electroosmosis (ICEO) [33].

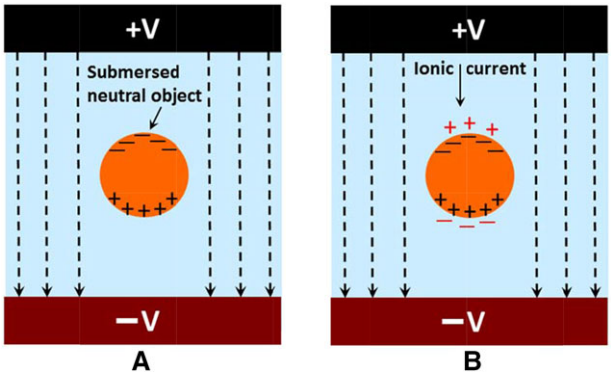

Figure 3. (A) Polarization of a submerged neutral object right after the application of an applied electric field. (B) Polarization of the object attracts opposite ions in the fluid and causes induced polarization of fluid at the interface of the object boundaries at time, t > 0. The time taken to form this induced polarization is known as charging time. The charging time depends on the fluid medium and characteristic length of the submerged object.

3 General governing equations for electrokinetics

3.1 Ion concentration and electric potential distribution in an electrolyte

In an electrolyte system, the distribution of ions depends on the applied or induced electric field. For a dilute solution, the mass concentration of species i can be obtained from the Nernst-Planck equation as [34]

$$\frac{\partial C_i}{\partial t} + \nabla \cdot N_i = S_i \tag{4}$$

where C is the mass concentration and S is the reaction term. The mass flux of each species can be obtained by balancing the frictional term with the advection and electromigration as

$$N_i = \vec{V} C_i + z_i \omega_i \vec{E} C_i - D_i \nabla C_i \tag{5}$$

Here D, z, ω are the diffusion coefficient, valence and absolute mobility of species, and $\vec{V}$ and $\vec{E}$ are the velocity and electric field, respectively. The electric field is related to the electrostatic potential as

$$\vec{E} = -\nabla\psi \tag{6}$$

The governing equations for the electric field can be obtained from Maxwell's equations by ignoring the magnetic effects. In a microfluidic channel with microelectrodes, the ratio of energy stored by the magnetic field to electric field can be given as [35]

$$\frac{U_m}{U_e} = \frac{\chi}{\varepsilon}\left(\frac{\vec{H}\cdot\vec{H}}{\vec{E}\cdot\vec{E}}\right) \tag{7}$$

where χ is the magnetic permeability and ε is the permittivity of the medium. The magnetic field $\vec{H}$ can result from conduction and/or displacement current. If the conduction

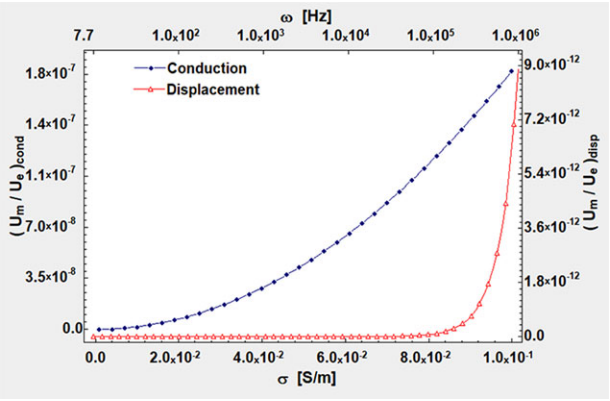

Figure 4. Relative magnitude of magnetic effect over electric for conduction and displacement current.

current dominates, the magnetic field can be approximated as $\sigma E L$; while for dominant displacement current, the magnetic field can be estimated as $\varepsilon\omega E L$ [35]. Figure 4 shows that for typical microfluidic setting, the magnetic energy is much smaller than the electrical energy if the applied electric field frequency is less than 100 MHz, and Maxwell's electromagnetic equations can be simplified as [36].

$$\nabla \cdot \vec{D} = \rho_e \tag{8}$$

$$\nabla \times \vec{E} = 0 \tag{9}$$

$$\frac{\partial \vec{D}}{\partial t} + \vec{J} = 0 \tag{10}$$

where $\vec{D}$ and $\vec{J}$ are the electric displacement vector and current density, and ρ_e is the total volumetric charge density. Equation (9) indicates that under the quasi-electrostatic condition, the electric field is irrotational. For a linear, isotropic and homogeneous medium, the material constitutive relation provides $\vec{D} = \varepsilon \vec{E}$. Thus, Eq. (8) can be rewritten as

$$\nabla \cdot (\varepsilon \nabla \psi) = -\rho_e \tag{11}$$

If ions are the major current carrier, the volumetric free charge density can be given as [37]

$$\rho_e = \sum_i e z_i c_i \tag{12}$$

where e is the electron charge.

One can obtain the charge conservation equation by performing divergence operation on Eq. (10) and by utilizing Eq. (8) as

$$\frac{\partial \rho_e}{\partial t} + \nabla \cdot \vec{J} = 0 \tag{13}$$

In an electrolyte system, the current density term consists of electromigration, diffusion, and advection (bulk flow) of charged species, which can be expressed as [38]

$$\vec{J} = F z_i \left(\sum \vec{V} C_i + z_i \omega_i \vec{E} C_i - D_i \nabla C_i \right) \tag{14}$$

where F is the Faraday constant. In an earlier work, Castellanos et al. [35] reported that, in most microfluidic system, the contribution of the diffusion and advection term is much smaller than the drift or electromigration term, and the charge conservation equation can be reduced to

$$\frac{\partial \rho_e}{\partial t} + \nabla \cdot \left(\sigma \vec{E} \right) = 0 \tag{15}$$

where the electrical conductivity is defined as $\sigma = F \sum z_i^2 \omega_i C_i$

3.2 Fluid flow and temperature distribution

The fluid flow in a channel is governed by the incompressible Navier-Stokes equations and continuity equation as [39]:

$$\rho_f \left(\vec{V}_t + (\vec{V} \cdot \nabla) \vec{V} \right) = -\nabla p + \mu \Delta \vec{V} + \vec{F}(\vec{r}, t) \tag{16}$$

$$\nabla \cdot \vec{V} = 0 \tag{17}$$

where ρ_f is the fluid mass density, $\vec{V}$ is the flow velocity, p is the pressure and $\vec{F}$ is the body force per unit volume. In Navier-Stokes equations, the first and second term of the left-hand account the transient and advective contribution in fluid flow, while the first and second terms on the right-hand side are related to pressure and viscous forces.

In most micro/nanofluidic system, the convective term is much smaller than the viscous term due to small length scale and ultra-low flow velocity. Thus, the advective term can be dropped from the Navier-Stokes equations, and it will not be discussed any further for the rest of the paper. However, the contribution of the remaining terms depends on the specific case. For instance, in time-periodic electrokinetic flow, the contribution of the transient term cannot be ignored. Similarly, in mixed pressure driven and electroosmotic flow [40], the contribution of the pressure term is very important. The body force might come from a number of sources, such as buoyancy force due to density difference [41], acoustic streaming [42–44], or electrokinetic force due to an electrical field [35]. In an electrical field driven flow, the electrokinetic body force term is primarily responsible for facilitating fluid pumping that arises due to the interaction between electric field and fluids.

The electrokinetic body force can be obtained from the Maxwell Stress Tensor (MST) which is regarded as the most reliable form to account for electric field driven forces [45]. The MST provides the comprehensive effect of electric field interactions among submerged particles and fluids. In most of the microfluidic electrokinetics, the frequency range for the applied electric field is low (less than 100 MHz) i.e. electric field wavelength is much higher than the typical electrode sizes. In such cases, the near field approximation holds and the effects of the magnetic field can be neglected, and the Maxwell stress tensor based on energy principles can be given by [46]

$$\vec{M}_M = \varepsilon \vec{E} \vec{E} - \frac{1}{2} E^2 \left[\varepsilon - \rho_f \frac{\partial \varepsilon}{\partial \rho_f} \right] \vec{I} \tag{18}$$

where $\vec{\vec{I}}$ is the unit tensor. The corresponding electrical field driven volumetric force density can be obtained by taking divergence as follows:

$$\begin{aligned}\vec{F} = \nabla \cdot \vec{\vec{M}}_M &= \nabla \cdot \left[\varepsilon \vec{E}\vec{E} - \frac{1}{2}E^2\left(\varepsilon - \rho_f \frac{\partial \varepsilon}{\partial \rho_f}\right)\vec{\vec{I}}\right] \\ &= \nabla \cdot \left(\vec{D}\vec{E}\right) - \nabla \cdot \left[\frac{1}{2}\left(\vec{E}\cdot\vec{E}\right)\varepsilon\vec{\vec{I}}\right] \\ &\quad + \nabla \cdot \left[\frac{1}{2}\left(\vec{E}\cdot\vec{E}\right)\rho_f \frac{\partial \varepsilon}{\partial \rho_f}\vec{\vec{I}}\right] \\ &= \rho_e \vec{E} - \frac{1}{2}\left|\vec{E}\right|^2 \nabla\varepsilon + \nabla\left[\frac{1}{2}\left|\vec{E}\right|^2 \rho_f \frac{\partial \varepsilon}{\partial \rho_f}\right]\end{aligned} \tag{19}$$

The first term on the right-hand side represents force due to the free bulk charges, the second term represents force due to polarization i.e. dielectric force, and the last term provides the force due to electrostriction. Depending on fluid medium and the applied electric field, one or more terms of the Eq. (19) can be neglected. The specific term that is significant for specific electrokinetic phenomena is discussed in the respective sections.

Application of electric field also causes Joule heating in the electrolyte, which can change the fluid temperature either locally or globally. The amount of heat generation depends on the electrical conductivity of the electrolyte as well as the applied electric field. The electric field driven temperature distribution can be obtained from the following energy balance equation [47]

$$\rho_f c_p \left(T_t + (\vec{V}\cdot\nabla)T\right) = \nabla\cdot(k\nabla T) + \Phi + \sigma(\vec{E}\cdot\vec{E}) \tag{20}$$

where c_p is the specific heat of the fluid, k is the thermal conductivity and Φ is the heat generation due to viscous dissipation. The viscous dissipation term is generally significant for highly viscous liquids. The last term on the right hand represents Joule heating [48] due to the applied electric field. Like the fluid flow equation, the advective term can be dropped from the energy equation for most micro/nanofluidic applications.

4 DC electroosmosis

Electroosmosis or electroendosmosis is the motion of ionized liquid relative to the stationary charged surface under the action of an applied electric field. This is also known as fixed charge electroosmosis or conventional electroosmosis. Figure 5 shows the working principle of electroosmosis in a straight channel. In this particular example, it is assumed that the microchannel surface acquires negative charges and cation dominant electric double layers are formed adjacent to the channel surface. The application of an electrical field will result in the movement of cations and anions towards cathode and anode, respectively. As the ions move in an applied electric field, it drags the fluid along it. Since, in Fig. 5, the EDL is rich in cations, there will be a net movement of fluid from the anode to the cathode.

Electroosmosis could be beneficial in some applications, such as in the transport of separated sample zone in isotachophoresis or it could be detrimental, as in the dispersion of protein bands in isoelectric focusing. In the separation process, the electroosmotic pumping can be controlled by modulating the surface charge characteristics.

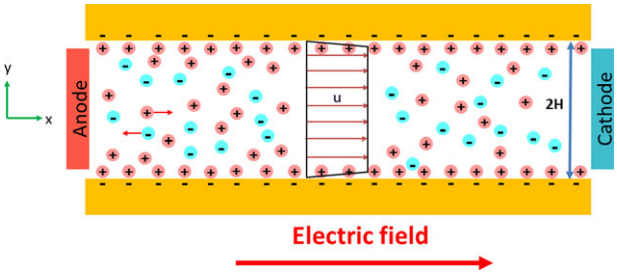

Figure 5. Schematic of conventional electroosmosis in a microchannel. Fluids move from anode towards cathode since the channel surface has negative charge density. The electric field exerts a tangential force on the electric double layer which is dominant in cations. This tangential force causes fluid to move. The electroosmotic mechanism can be applied in micro and nanochannel to pump fluids for various bioanalytical applications without any mechanical components.

Electric field induced electrokinetic body force is primarily responsible for electroosmosis. If we assume that the fluid medium is homogeneous throughout the channel, the electrokinetic body force can be approximated as $\rho_e\vec{E}$. This body force is only dominant in the EDL region since the region outside of the EDL is electrically neutral. For pure electroosmotic flow through a channel, it is possible to obtain an analytical solution for flow velocity by balancing the body force term with the viscous term as [40]

$$u(y) = -\frac{\zeta\varepsilon}{\mu}E_x\left(1 - \frac{\psi(y)}{\zeta}\right) \tag{21}$$

where ψ is the electric potential in the fluid, E_x is the tangential electric field, y is the coordinate measuring from the channel centerline, and ζ is the zeta potential. At the channel surface, the electric potential approaches zeta potential, and the flow velocity approaches zero in order to satisfy the no-slip boundary condition at the channel surface. For a thin EDL case, the electric potential drops to zero for most of the channel, and the flow velocity can be approximated as uniform throughout the channel with the Helmholtz-Smoluchowski velocity

$$u_{HS} = -\frac{\zeta\varepsilon}{\mu}E_x \tag{22}$$

For most microfluidic applications, the EDL region (0.1–10 nm) is much smaller than the channel height (10–100 microns). Thus, for those flows, electroosmotic flow can be modeled with the Helmholtz-Smoluchowski slip velocity at the channel wall. However, for the nanofluidic channel, where the channel size is comparable to the electric double layer, one should avoid the prescription of Helmholtz-Smoluchowski slip velocity at the channel wall. Rather, no slip and no penetration boundary conditions should be exercised in those cases.

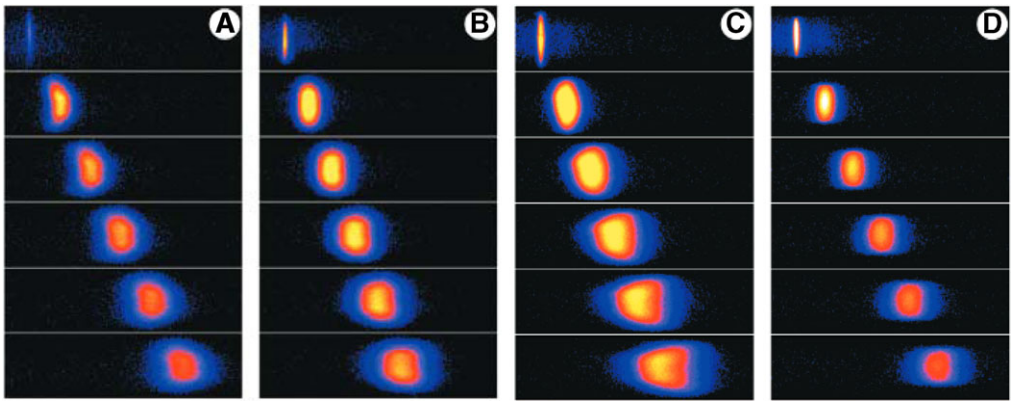

Figure 6. Fluorescent dye images of electroosmotic flow in various types of channels. (A) Acrylic microchannel at 266 V/cm, (B) PDMS microchannel at 248 V/cm, (C) hybrid acrylic/PDMS microchannel at 245 V/cm, and (D) Fused-silica capillary at 250 V/cm. In all cases, the time gap between successive images is 50 ms. Different material types have different surface charge density and hence zeta potential, which is the primary reason for different flow velocity. The results are reproduced from Ross et al. [49].

The electroosmotic flow velocity equation indicates that the nature of flow will depend on the type of channel materials since zeta potential is an indicator of surface charge density. The effect of substrate types on the EOF velocity profile is shown in Fig. 6 [49]. For PDMS and fused-silica capillary microchannel, the flow is plug like, while for hybrid acrylic/PDMS microchannel, there is higher velocity in the middle of the channel compared to the edge. Authors hypothesized that this flow pattern variation from plug-like velocity is due to different surface charge densities at the top and bottom layer as well as due to the temperature variation caused by different thermal conductivities of acrylic and PDMS materials. Sinton et al. [50] also reported that EOF velocity deviates from plug-like flow if there is a non-uniform temperature distribution in the channel.

In electroosmotic flow through a microfluidic channel, the non-uniform surface charge density can create an adverse or favorable pressure gradient. At steady state, this combined electroosmotic and pressure-driven flow can be estimated by adding a pressure driven flow component as [51]

$$u(\mathrm{y}) = -\frac{\zeta\varepsilon}{\mu}\mathrm{E_x}\left(1-\frac{\psi(\mathrm{y})}{\zeta}\right) - \frac{\mathrm{H}^2}{2\mu}\frac{\mathrm{dP}}{\mathrm{dx}}\left(1-\frac{\mathrm{y}^2}{\mathrm{H}^2}\right) \tag{23}$$

where H is the channel half height. For a favoarable (adverse) pressure gradient, the dP/dx is negative (positive).

4.1 DC electroosmosis as pumping mechanism

In last two decades, the electroosmotic flow has been studied extensively both experimentally and theoretically. Dutta et al. [51] have presented the pressure building ability of DC electroosmotic flow using a hybrid microchannel consisting of materials with different surface electrical properties (zeta potential). Similar conclusions were obtained from the experimental works of Herr et al. [52].

Electroosmosis in microfluidics is mainly used to transport species or generate fluid flow [53]. Table 1 shows a few selected electroosmotic pumping works carried out by various researchers in last two decades. The maximum pressure generated by an electroosmotic pump can be expressed as

$$\Delta P_{\max} = \frac{8\varepsilon\zeta}{d^2}\Delta\phi \tag{24}$$

where d and $\Delta\phi$ are the channel diameter and applied potential difference. Thus, the pumping power of an electroosmotic pump can be raised by increasing the zeta potential, the permittivity of the medium and the applied electric field, or by decreasing the tube diameter. Various researchers have tried to maximize the pressure building ability by modulating different parameters with various degrees of success. The use of nanofluidic channel is the most popular method since there has been enormous interest in the development of the nanostructured devices. However, the flow rate supplied by the nanofluidic channel is sometimes not adequate; 10 to 1000 of nanofluidic channels are needed to maintain the desired flow rate. Based on the nanochannel design and fabrication processes, the electroosmotic pump can be classified as open channel, packed-column, porous membrane, porous monolith, etc. In the following section, we report different types of classical electroosmotic pump that have been used in microfluidic devices as a pumping mechanism.

4.1.1 Open-channel electroosmosis

This type of electroosmotic pump is generally composed of 10 to 1000 open parallel microchannels or capillaries to provide fluid flow in a large diameter channel. Figure 7 shows the basic structure of such a micropump as presented in the work of Lazar and Karger [58], where they microfabricated a pump with numerous microchannels. Authors claimed to obtain a flow rate ranging from 10 to 400 nL/min using 1–100 microchannels. They also provided an expression for pressure generated by open channel electroosmotic pump as [58]

$$\Delta P = \frac{32\, n\,\varepsilon\, d_1^2 E_1}{n\frac{d_1^4}{L_1} + \frac{d_2^4}{L_2}} \tag{25}$$

Table 1. Comparisons of various electroosmotically driven micropumps

Author and year	Flow rate	Max pressure	Applied voltage	Pore size	Pump type
Gan et al. 2000 [54]	3.0 mL/min	0.15 MPa	500 V	2–5 μm	Porous-membrane
Zeng et al. 2001 [55]	3.6 μL/min	20 atm	2 kV		Packed-column
Yao et al. 2001 [56]	7 mL/min	2 atm	200 V		Open-channel
Zeng et al. 2002 [57]	0.8 mL/min	2 atm	1.0 kV		Packed-column
Lazar et al. 2002 [58]	10-400 nl/min	80 psi	2 kV		Open-channel
Chen et al. 2002 [59]	15 μL/min	0.33 atm	1 kV		Open-channel
Laser et al. 2002 [60]	13 μL/min	6 kPa	400 V		Open-channel
Takamura et al. 2003 [61]	415 nl/min	800 Pa	10 V		Open-channel
Yao et al. 2003 [62]	33 mL/min	1.3 atm	100 V	1.2 and 0.55 μm	Porous-membrane
Laser et al. 2003 [63]	170 μL/min	10 kPa	400 V		Open-channel
Tripp et al. 2004 [64]	0.41 mL/min	0.38 MPa	50 V	1700 nm	Porous monolith
Razunguzwa et al. 2004 [65]	2 μL/min		3 kV		Packed-column
Chen et al. 2005 [66]	4.2 μL/min	26 MPa	8 kV		Packed-column
Brask et al. 2005 [67]	6 μL/min	450 KPa	30 V	200 nm	Porous-membrane
Chen et al. 2005 [68]	0.4 μL/min	0.4 MPa	6 kV	micrometer	Porous monolith
Yao et al. 2006 [69]	3.2 mL/min	30 kPa	25 V	1 to 3 μm	Porous-membrane
Wang et al. 2006 [70]	2.9 μL/min	3 atm	6 kV	4 μm	Porous monolith
Nie et al. 2007 [71]	0.1 μL/min	2.4 bar	2 kV		Porous monolith
Nie et al. 2007 [72]	400 nl/min		2 kV		Porous monolith
Miao et al. 2007 [73]	86 mL /cm^2 min		70 V	50-200 nm	Porous monolith
Vajandar et al. 2007 [74]	0.125 mL/min-V/ cm^2		3 V	30–100 nm	Porous membrane
Seibel et al. 2007 [75]	10 nl/ min	65 Pa	40 V		Microchannel
Joo et al. 2007 [76]	262.4 nl/min		1 kV/cm		Open-channel
Wallner et al. 2007 [77]	11.9 μL/min/mm^2	5.2 kPa	60 V	>500 μm	Porous membrane
Edwards et al. 2007 [78]	0.19–2.30 μl/min		40–400 V		Open channel
Chen et al. 2008 [79]	0.09 mL/min V/ cm2	25 kPa	20 V	20, 100 and 200 nm	Porous membrane
Borowsky et al. 2008 [80]	20 to 70 nl/min	800 psi	1.5-4.5 kV	50 μm	Porous monolith
Berrouche et al. 2008 [81]	13.6 mL/min	2 kPa	150 V		Nanoporous
Chen et al. 2008 [82]	2.125 μL/min	42 MPa	4 kV		Packed-column
Ai et al. 2010 [83]	275 μL/min		5 V	200 nm	Porous membrane
Shin et al. 2011 [84]	5-30 μl/min	7 kPa	0.2-0.8 V	1 μm	Porous membrane
Nagarale et al. 2011 [85]	26 ± 3 μL/min		1 V	0.7-1 μm	Porous membrane
Gu et al. 2012 [86]	287 nl/min	1208 bar	10 kV	700 nm	Porous monolith
Cao et al. 2012 [87]	5 mL/min	900 Pa	11 V	5 micron	Open-channel
Luong et al. 2013 [88]	0.7 mL/min	9×10^4 Pa	7.5 V	3.2 μm	Porous medium
Parashchenko et al. 2014 [89]	325 μL/min		300 V	8-9 μm Channel dia	Porous membrane
Li et al. 2016 [90]	122 pL/s		50 V	80 μm Channel dia	Microchannel

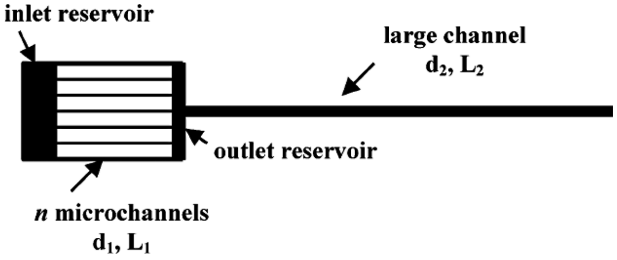

Figure 7. Schematic of an open channel electroosmotic pumping system used for eluent gradients. Here *n* number of microchannels of diameter d_1 and length L_1 are connected between two reservoirs. A larger diameter (d_2) channel of length L_2 is connected to the outlet reservoir. Electroosmotic pumping mechanism results from the application of electric field between inlet and outlet reservoirs, and no electric field is applied to the fluid of larger diameter channel. Reprinted with permission from Lazar and Karger [58]. Copyright (2002) American Chemical Society.

where L_1 is the applied electric field in the narrow channels. The discharge of such a pump can be obtained as

$$Q = \frac{\frac{L_1}{L_2}\left(\frac{n\pi d_1^2}{4}\frac{\varepsilon\zeta}{\mu}E_1\right)}{\frac{L_1}{L_2} + n\left(\frac{d_1}{d_2}\right)^4} \tag{26}$$

These model equations are in good agreement in predicting their experimental results. Adopting similar concept, Darabi et al. [91] developed an electroosmotic micropump using numerous open channels to cool down an electronic chip. Reichmuth et al. [92] presented an open channel EOF pump for HPLC separation by increasing the dielectric constant of the working fluid. Their new design improved the pressure generation and efficiency up to 85 and 140%, respectively. Similar high pressure, larger flow rate, higher efficiency open channel electroosmotic micropumps are reported by [56, 76, 78, 87, 93].

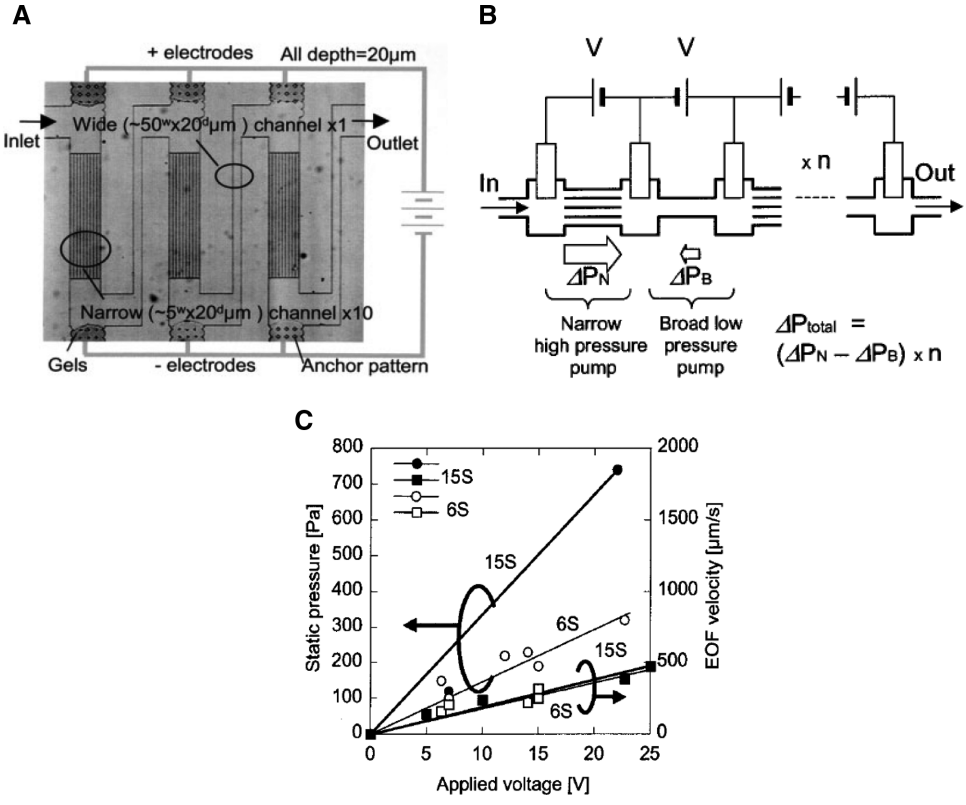

Figure 8. (A) Photograph of a cascade type of EOF pump, (B) fundamental pressure building capability using a lower electric field, and (C) performance of cascade type open channel electroosmotic pump with 15 and 6 stages. In Fig. C, symbol circle represents pressure, while symbol rectangle is for electroosmotic flow velocity. Reproduced with copyright permissions from Takamura et al. [61].

A cascade electroosmotic pump consisting of multiple narrower (5 μm × 20 μm) and wider (50 μm × 20) channels was reported by Takamura et al. [61] as shown in Fig. 8. The main objective of their micropump is to operate at low voltage to avoid Joule heating as well as bubble formation by serially connecting a number of pumping blocks, where the total applied potential difference remains same as in one block. Each pumping block consists of narrow channels and a wide channel (Fig. 8A), and the configuration for applied electric potential is shown in Fig. 8B. According to their unique design, a larger favorable pressure gradient can be developed in narrower channels, while much smaller adverse pressure gradient is formed in the wide channel. Thus, the total pressure difference in each module can be obtained by subtracting the pressure required in the wide channel from the pressure generated in narrower channels. Figure 8C shows the pressure developed by a cascade EOF pump for different applied electric potential. Their experimental results show that pressure is higher with increased number of stages, but the fluid velocity remains the same at both the 6 and 15 stages for a particular electric field.

4.1.2 Packed-column electroosmosis

In packed-column EOF pump, a capillary is filled with micron-sized particles and the capillary ends are sealed by frits like electrochromatography column. Paul et al. 1998 [94] have demonstrated the feasibility of a packed column micropump, where they obtained pressure in excess of 8000 psi using micron size particles. Later, Zeng et al. 2001 [55] developed a packed column micropump and presented the performance of the electrokinetic pump using a setup similar to regular pump testing station (Fig. 9A).

As shown in Fig 9B, in a packed column electroosmotic pump, the flow rate can be increased by increasing the applied voltage for a fixed back pressure. The small nonlinearity in experimental flow rate vs applied voltage was due to a slight variation of the back pressure in their experiments. Figure 9C shows pump curve for the packed column electroosmotic pump, where they observed bubbles when back pressure is below 7 atm. The pump discharge remains constant in this bubble formation region. Their pump was capable of producing a maximum flow rate of 17 μL/min and a maximum pressure of 20 atm. Later, a number of researchers integrated the packed-column electroosmotic pumps with HPLC, liquid chromatography, nanoflow gradient generator, and ion exchange beads for various operating pressure and flow rate [57, 65, 66, 82, 95, 96].

4.1.3 Porous membrane electroosmotic pump

In this type of pump, a porous membrane is utilized to construct the main functional unit of the pump. This porous membrane contains numerous tortuous channels that are connected from one side of the membrane to the other [97]. Unlike packed column electroosmotic pump, the length of

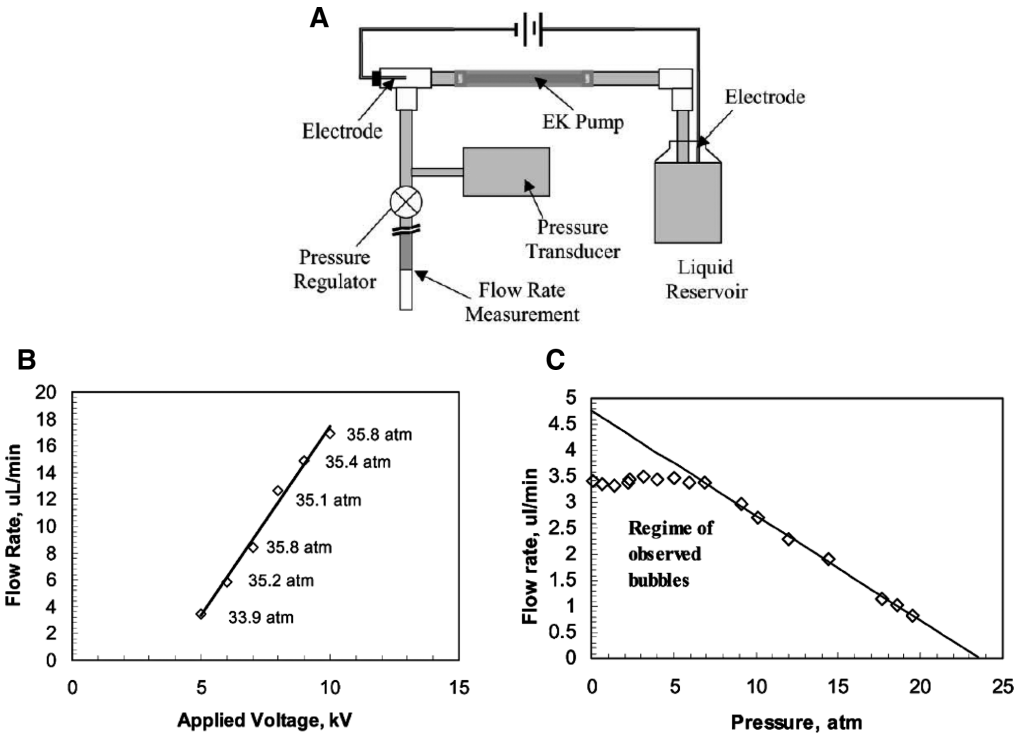

Figure 9. (A) Schematic of the pumping section of a packed column electroosmotic micropump and the test rig to characterize a packed column electroosmotic micropump. The electric field is applied using two platinum electrodes. Pressure transducer and pressure regulator were used to measure the flow rate and the pressure, respectively; (B) Flow rate vs applied voltage at a fixed back pressure; (C) Pump curve (flow rate versus back pressure) for an applied potential difference of 2 kV. The pump's column is 5.4 cm long, 530 μm in diameter, and it is filled with 3.5 μm silica particles. DI water (pH = 5.7, σ = 3.0 μS/cm) was used as the working fluid in this pump. Reproduced with copyright permissions from Zeng et al. [55].

the channels in a porous membrane is much shorter [62]. Thus, a much higher electric field can be achieved with low applied voltage.

Miao et al. [73] demonstrated a porous membrane electroosmotic micropump, where the membrane is fabricated by anodization of aluminum foils in acidic solution. Figure 10C illustrates a schematic of their micropump, while Figs 10A and 10B show the images of the highly arranged nanochannels. The core pumping (membrane) section is fixed with plates on both sides to withstand the pressure generated by the electroosmotic pump, and it is placed between the inlet and outlet reservoirs. An electric potential difference of 0.1 to 70 V is applied to gold or platinum electrodes on the two sides of the membrane. They reported almost linear flow rate increase with an electric field (Fig. 10D), and for a particular applied electric field, the largest diameter pore provided highest flow rate. By changing the anodization process, they were able to obtain nanochannels of different diameters ranging from 5 to 280 nm for their membranes. Moreover, they presented a way to improve the flow rate by treating the channel surface with different chemicals, which improves the surface electrical characteristics for electroosmotic pumping. For instance, they reported that silica coated nanochannels can produce 108 times larger flow rate than the untreated nanochannel.

Similar porous silicon membrane based electroosmotic pumps are reported in [54, 67, 77, 84, 85, 89, 98] for various flow rate, pressure and applied electric fields. The performance of the pump depends on porosity, zeta potential, and pore's sizes. Yao et al. [98] reported a maximum flow rate of 3.2 mL/min and a maximum pressure of 730 Pa for a 350 μm thick silicon membrane, with pore sizes of 3 and 1 μm, respectively. For a fixed applied voltage, Chen et al. [79] have shown that flow rate can be increased by increasing the pore size. However, if the membrane size is very thin, then droplets may generate at low voltages [99]. Soumitra et al. [100] modified the zeta potential of the pores' inner surface by depositing different coating materials to control flow.

4.1.4 Porous monolith electroosmosis

In this case, a monolith column is used as a pumping component. Unlike a packed column or a porous membrane electroosmotic micropump, frits are not required in a monolith electroosmotic pump [101]. Organic polymer or inorganic silica-monolith can be used for the development of porous monolith electroosmotic pump [70, 102]. Tripp et al. 2004 [64] fabricated electroosmotic pumps based on microporous polymer monoliths. They investigated the effect of pore sizes on

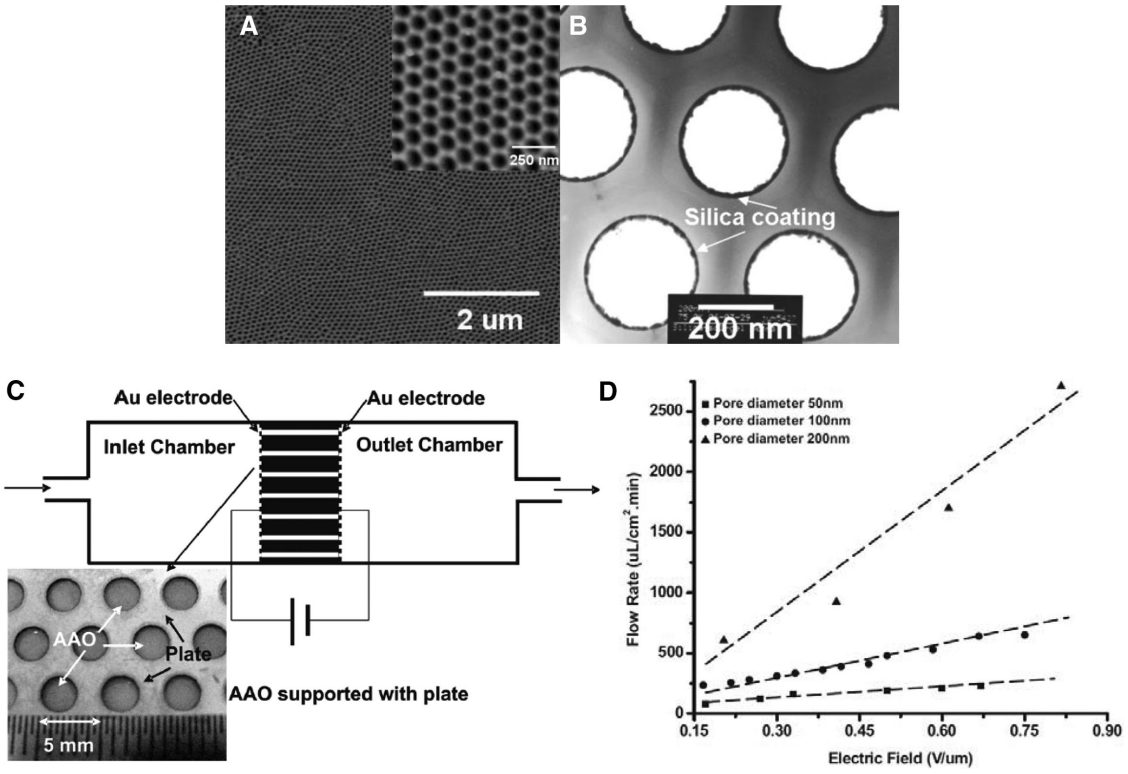

Figure 10. Porous membrane electroosmotic pump and its performance. (A) Images of nanochannels obtained from SEM and AFM (inset figure), (B) nanochannel coated with silica for augmenting the flow rate, (C) schematic of a porous membrane electroosmotic nanopump. Electrodes were formed on the two sides of the membrane using a thin film deposition of Au or Pt, while the nanochannel structure is formed by the anodization of aluminum foil, and (D) flow rate supplied by the electroosmotic pump at different electric field for various pore diameter. Diameters of nanochannels can be varied between 5 to 280 nm by controlling the anodization process. Reproduced with copyright permissions from Miao et al. 2007 [73].

the monoliths, crosslinking density, and applied voltage on flow rate and pressure. Their electroosmotic pump can generate a flow rate of 0.41 mL/min and the measured pressure was about 0.38 MPa. Similar porous monolith based electroosmotic pumps are also reported by other groups [103, 105]. Gu et al. 2012 [86] reported the assembly of multiple monolith electroosmotic pump in series, while Nie et al. 2007 [71] reported the assembly of nine parallel electroosmotic pumping systems for higher flow rate and pressure. Porous monolith electroosmotic pumps are used for various applications, such as flow injection system [68], liquid preconcentration and delivery process [72], and the separation of explosive molecules [80].

5 AC electroosmosis (ACEO)

Similar to DC electroosmosis, discussed in the previous section, AC electroosmosis can drive the bulk fluid through the interaction of double layers and external electric fields. However, in AC electroosmosis, a time-periodic electric field is applied between a pair of neighboring electrodes as shown in Fig. 11. The charging of these electrodes with an AC current not only provides the tangential component of electric field, but also the surface charges on the electrodes for the creation of EDL. During the first half of the AC electric signal (Fig. 11A), the polarities of left and right electrodes are positive and negative, respectively. Thus, the electric field (green line) is from the left electrode to the right one during the first half cycle. Moreover, the positively polarized left electrode creates an EDL parallel to the electrode which is dominant in anions, while the negatively polarized right electrode generates a cation-rich EDL. Hence, anions on top of the left electrode moves opposite to the electric field direction and cations on top of the right electrodes drift along the direction of electric field. During the second half of the AC signal (Fig. 11B), the left electrode becomes negatively polarized and right electrode gets positively polarized. This polarity change reverses the electric field direction as well as the dominant type of ions on both electrodes causing movement of ion in the left direction on the left electrode and towards the right direction on the right electrodes. In other words, in both half cycles, the direction of ion movement remains the same. This ion movement carries surrounding fluids owing to the viscous drag. AC electroosmosis requires much lower voltage than DC electroosmosis, which is one of the major advantages of this technique. Moreover, the effect of AC electric field can be controlled by the waveform,

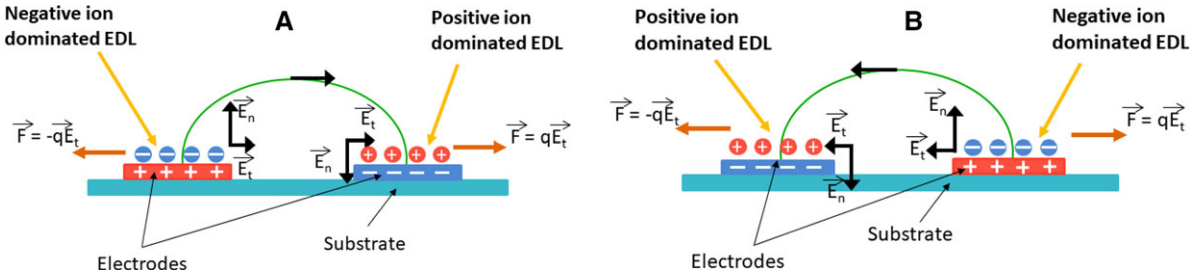

Figure 11. ACEO fluid motion and induced charges at electrode surfaces. (A) During the half cycle when the left electrode has positive polarity and the right electrode has negative polarity; (B) during the next half cycle with opposite electrical polarity. In AC electroosmosis, the bulk electrolyte is electroneutral and behaves in a resistive manner, while the EDL is charged and behave like a capacitor.

peak to peak voltage and the frequency of the applied electric potential.

Although there are many similarities between AC and DC electroosmosis, there are some significant differences between them. For instance, in AC electroosmosis, electrodes are responsible for both creating the electric field as well as forming the EDLs. In regular or DC electroosmosis, the channel surface charges actively participate in the EDL formation, and the surface charge density is much lower than in AC current supplying electrodes patterned on the channel surface. Thus, the mechanism for the electric double layer formation is quite a bit different in AC electroosmosis, which is discussed in Section 2.2.

The general governing equations for fluid velocity and electrostatic potential are same as in DC electroosmosis. Thus, we briefly review the boundary conditions for electric potential as well as for the flow field in the following section. Ramos and coworkers [105] presented the mathematical model to study the AC Electroosmosis considering the thin double layer and linear double theory. Later, Kilic et al. [32] extended the theory for the nonlinear electrokinetics, where the potential difference across the electric double layer is much larger than the thermal potential. AC electroosmosis takes place when the applied electric field frequency is much smaller than the charge relaxation frequency of the bulk electrolyte $f_c = \sigma/2\pi\varepsilon$. At this low applied electric field frequency range, the EDL is in quasi-equilibrium. Under this assumption, the EDL goes through capacitive charging, while the bulk of the electrolyte behaves in a resistive manner. Thus, one can model the fluid domain with Laplace equation (can be deduced from Eq. (11)), but with appropriate boundary conditions. At the channel surface, such as in the glass, PMMA, or PDMS, an electrically insulating boundary condition is valid. However, at the electrode surface, the boundary condition is slightly more complicated due to EDL formation. It is not possible to apply a Dirichlet boundary condition. The reason is that at low frequencies the EDL will go through capacitive charging and there will be a potential drop across EDL.

The charging of the double layer due to bulk current can be expressed as [106]

$$\sigma\frac{d\psi}{dy} = \frac{\partial q_{DL}}{\partial t} = i\omega q_{DL} \tag{27}$$

where, $q_{DL} = C_{EDL}(\psi - V_e)$ and C_{EDL} is the capacitance per unit area of the electric double layer (both Stern and diffuse layer), V_e is the potential applied to the electrode, and ψ is the electric potential at the outer side of the diffuse layer. This linear relationship is valid for a small potential difference across the electric double layer. The double layer capacitance can be found from

$$\frac{1}{C_{EDL}} = \frac{1}{C_S} + \frac{1}{C_D} \tag{28}$$

where C_S and C_D are the Stern and diffuse layer capacitance. The capacitance of the Stern layer is generally independent of the ionic concentration of the solution. The capacitance of the diffuse layer can be found as [32]

$$C_D(\psi_D) = -\frac{dq}{d\psi_D} \tag{29}$$

where ψ_D is the diffuse layer potential. Kilic et al. [32] presented expressions for the diffuse layer capacitance considering the different level of double layer charging based on the applied electric potential as.

$$C_D = \frac{\varepsilon}{\lambda_D}\frac{1}{\sqrt{2\upsilon}\sqrt{\left(1-\frac{\upsilon}{2}\right)^2 + \frac{ze|\psi_D|}{k_BT} - \ln\left(\frac{2}{\upsilon}\right)}} \qquad \psi_D > \psi_c$$

$$C_D = \frac{\varepsilon}{\lambda_D}\mathrm{Cosh}\left(\frac{ze\psi_D}{2k_BT}\right) \qquad \psi_D << \psi_c$$

where υ is the volume fraction occupied by ions in the bulk fluid.

AC electroosmotic flow velocity can be obtained from the solution of the Navier-Stokes and continuity equations by neglecting the inertia term. The inertia term consists of the transient term as well as the advective term. The transient term can be dropped since the time scale for fluid to respond to an applied AC electric field is much smaller than the applied electric field time scale. For instance, the typical electric field frequency used for AC electroosmosis is 10–100 kHz, while the typical response time for fluid in AC electroosmosis is in milliseconds. The advective term can be dropped because of the fact that the flow velocity is very small in an electric field driven micro/nanochannel flow. The typical Reynolds

number for microflows is much smaller than 0.01. Thus, the simplified governing equations for AC electroosmosis are

$$\nabla p = \mu \Delta \vec{V} + \vec{F}(\vec{r}, t) \tag{30}$$

$$\nabla \cdot \vec{V} = 0 \tag{31}$$

These flow equations can be solved with no-slip and no-penetration boundary conditions at the channel and electrode surfaces, and periodic boundary conditions at the appropriate symmetry planes. In this general formulation, one has to find the forcing term throughout the computational domain. Like DC electroosmosis, for incompressible flow with a homogeneous fluid, the predominant forcing term is Coulombic. However, the computation of the Coulombic forces requires detail modeling of the EDL for electric potential distribution. One alternative approach is to solve the flow equations without the forcing term, but with an appropriate electroosmotic slip velocity at the electrode surfaces. For AC electroosmotic, the required slip velocity at the channel surface can be given as

$$u_t = -\frac{\varepsilon}{\mu}\left[\left(\tilde{\phi} - \tilde{\psi}\right)\tilde{\tilde{E}}_t\right] \tag{32}$$

where $\tilde{\phi}$ is the complex electric potential at the inner side of the diffuse layer, and $\tilde{\tilde{E}}_t$ is the tangential (complex) electric field. In linear regime [106], capacitances and electric potential can be related by

$$\frac{C_{EDL}}{C_D} = \frac{Diffuse\ layer\ potential\ drop}{Total\ double\ layer\ potential\ drop}$$

$$= \frac{\left(\tilde{\phi} - \tilde{\psi}\right)}{\left(\tilde{V}_e - \tilde{\psi}\right)} = \frac{\psi_D}{\left(\tilde{V}_e - \tilde{\psi}\right)} \tag{33}$$

Using Eqs. (32) and (33), the time-averaged AC electroosmotic velocity can be obtained as

$$\langle u_t \rangle = -\frac{\varepsilon}{2\mu}\frac{C_{EDL}}{C_D^{\nu}}\mathrm{Re}\left[\left(\tilde{V}_e - \tilde{\psi}\right)\tilde{\tilde{E}}_t^{*}\right] \tag{34}$$

where Re[] is the real component and $\tilde{\tilde{E}}_t^{*}$ is the complex conjugate of the electric field.

5.1 ACEO as Pumping Mechanism

In ACEO pumps, an electric field is applied through microelectrodes patterned on the channel surface. Generally, symmetric coplanar electrodes are used for this type of pumping as shown in Fig. 12A. Figures 12B–D illustrate the experimental work of Green et al. [107], where they studied the effect of applied electric potential magnitude and frequency in pumping KCl solution of different conductivity: Fluid A – 2.1 mS/m, Fluid B – 8.6 mS/m, and Fluid C: 84 mS/m. Flow velocity was measured with fluorescent tracking particles under microscope and images were recorded. Their experimental results show that the ACEO velocity increases with frequency and reach to a peak value before decreasing with frequency. ACEO reaches to a negligible value at a frequency known as charge relaxation frequency. Thus, for AC electroosmotic flow, the applied frequency range should be

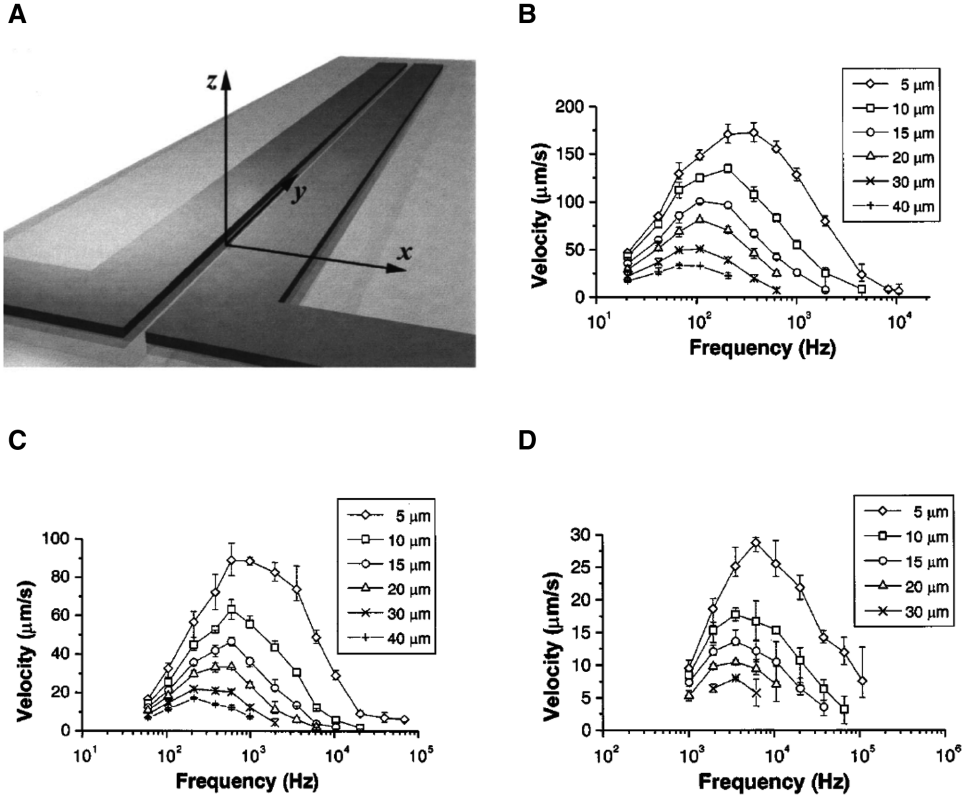

Figure 12. (A) Schematic of coplanar electrodes used for ACEO. Step averaged velocity obtained from experiments at different frequencies for KCl solution with conductivity (B) 2.1 mS/m, (C) 8.6 mS/m and (D) 84 mS/m. Results are obtained for different x-location along the channel as noted in the figure. Each electrode is 2 mm long, 200 microns wide and 130 nm (10 nm Ti, 100 nm Au, and 20 nm Ti) high, and the gap between electrodes is 25 microns, and applied potential is 2 V. Reprinted figures with permission from Green et al. [107]. Copyright (2000) by the American Physical Society.

smaller than the charge relaxation frequency so that the EDL can form on top of the electrode surface. In addition, they observed that flow velocity decreases with the conductivity of the fluid indicating that the AC electrothermal velocity is negligible for the frequency range considered in their work. Similar planar electrode based ACEO pump was reported by other researchers [108, 109] to name a few. Urbanski et al. 2007 [110] developed 3D ACEO pumps based on nonplanar electrodes with variable heights. They demonstrated that nonplanar ACEO pump can produce fast fluid flow compared to planar ACEO pumps.

Although symmetrical electrodes are popularly used to create AC electroosmotic flow, ACEO pumping with symmetrical electrodes cannot create a flow in a preferred direction. In fact, this type of symmetrical electrode configuration creates a circulating motion in the vicinity of an electrode in the form of vortices. Ajdari [111] first theoretically predicted that the asymmetry of electrodes array can be used to drive fluid in a certain direction for pumping liquid in microfluidics. In their theoretical work, they have demonstrated asymmetry by modifying the surface charge characteristics of electrodes in addition to electrode/channel surface topology. Later, Mpholo et al. [112], Brown et al. [113], Ramos[115] and others experimentally demonstrated pumping of fluid using asymmetric electrodes in the microchannel.

Figure 13 shows the electrode arrangements for an AC electroosmotic pumping with an asymmetric electrode array. The asymmetric electrode array consists of wide electrodes (E_1), narrow electrodes (E_2), narrow gaps (G_1) and wide gaps (G_2) between electrodes. In order to break the symmetry, the width of the narrow electrode should not be the same as the width of the wide electrode. In addition, the gaps G_1 and G_2 should be different [115]. Ramos et al. [114] studied the asymmetric ACEO numerically where they have shown fluid flow is always in one direction, but the experimental work from the same group for the identical microfluidic setup was not conclusive [116]. For instance, outside the vortices region, they obtained flow from the right to the left direction for low applied electric potential, but their flow direction reverses at high applied electric field direction (not shown). Pure AC electroosmotic phenomena with the linear voltage drop across the double layer cannot be used to justify the flow reversal at the high applied AC potential, and some other electric field driven mechanism might be responsible. Storey et al. [117] identified the steric effects, overcrowding of ions due to the large induced voltage across the double layer, related decrease in surface conductance as the primary reason for flow reversal even at the low bulk salt concentration case. Nevertheless, the average flow velocity obtained in both high and low electric field cases are negligible for any useful pumping in a preferred direction.

To improve the pumping ability of ACEO pump, Huang et al. [118] presented an ACEO pump with stepped electrode arrays, and they compared their design with a traditional asymmetric coplanar electrode ACEO micropump. Their pump could generate a pressure 1.3 kPa at 1 V_{rms} and 1 kHz, which is two orders of magnitude higher than the previously reported ACEO micropumps. Although the stepped design presented in their work was able to improve the pumping ability significantly, it is paltry for any useful pumping in a microfluidic device. In other words, AC electroosmotic phenomenon cannot be used as a standalone global pumping technology, rather it can be employed as a local control mechanism since it creates highly nonuniform velocity, which is responsible for vortices. Researchers combined the ACEO local pumping with other phenomena such as dielectrophoresis [119], light activated phenomena [120], pressure driven flow, etc. for separation, concentration, manipulation, and sensing. For instance, ACEO pumping is combined with dielectrophoresis for the collection of cells [121] and particles [122], separation of colloids [123], rotation [124] and manipulation [125] of particles in a microfluidic chip. Similarly, by combining with other microfluidic-based actuation technique, ACEO pumping is used for separation and concentration [126–129] and detection [130–133].

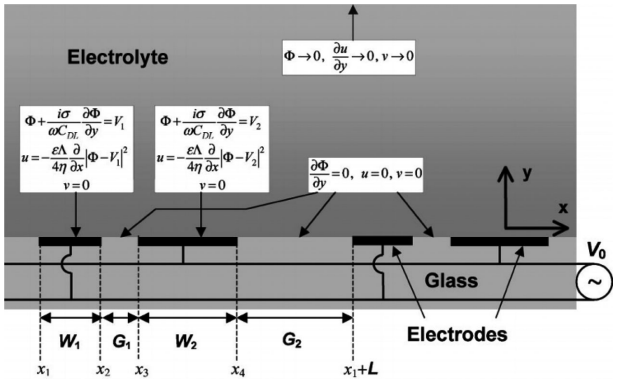

Figure 13. Schematic of the asymmetric electrode array for net fluid flow in a preferred direction. Boundary conditions for electric field and flow field are also presented for numerical simulation of ACEO. Reprinted this figure with permission from Ramos et al. [114]. Copyright (2003) by the American Physical Society.

6 AC Electrothermal

AC electrothermal effect is caused by the interaction between the applied electric field and space charges created by the temperature gradient driven conductivity and permittivity variations. Like ACEO, generally co-planar electrodes are used for creating ACET flow. The non-uniform electric field generated by the coplanar electrodes can generate spatially varying heat sources in the fluid domain, which in turn causes nonuniform temperature distribution in the system. Since the fluid properties, such as density, viscosity, electrical conductivity, and permittivity are a function of temperature, non-uniform temperature field will create a permittivity and density gradient, and these gradients will contribute to the forcing term, in addition to the Coulombic force. Like EO and ACEO, the electrostriction term is negligible for ACET flow. Thus, the

total forcing term (per unit volume) can be expressed as a superposition of electrical and buoyant force.

$$\vec{F} = F_{elec} + F_{bouy} = \rho_e \vec{E} - \frac{1}{2}\left|\vec{E}\right|^2 \nabla\varepsilon + (\rho - \rho_r)\vec{g} \tag{35}$$

where ρ_r is the reference density and $\vec{g}$ is gravitational acceleration.

Since AC electric field is used in ACET, the computation of electrical forcing term requires the solution of the complex electric field, which is computationally expensive. Ramos et al. [25, 35] have introduced an alternate method for calculating flow field in ACET using some reasonable approximations. For instance, it is assumed that the electric double layer is very thin and the bulk region is electrically neutral. In their analysis, the total electric field $\vec{E}$ is decomposed into two components, $\vec{E}_0$ and $\vec{E}_1$, where

$$\left|\vec{E}_0\right| >> \left|\vec{E}_1\right| \tag{36a}$$

$$\nabla \cdot \vec{E}_0 = 0. \tag{36b}$$

Using aforementioned relationship, the electrokinetic body force term can be approximated as

$$\vec{F} \cong \rho_e \vec{E}_o - \frac{1}{2}\left|\vec{E}_0\right|^2 \nabla\varepsilon \tag{37}$$

Similarly, the free charge density can be rewritten as

$$\begin{aligned}\rho_e = \nabla \cdot \left(\varepsilon \vec{E}\right) = \nabla\varepsilon \cdot \vec{E}_0 + \varepsilon\nabla \cdot \vec{E}_0 + \nabla\varepsilon \cdot \vec{E}_1 \\ +\varepsilon\nabla \cdot \vec{E}_1 \cong \nabla\varepsilon \cdot \vec{E}_0 + \varepsilon\nabla \cdot \vec{E}_1\end{aligned} \tag{38}$$

To find the electrokinetic forcing term, one has to find both $\vec{E}_0$ and $\vec{E}_1$. Fortunately, $\vec{E}_0 = -\nabla\psi_0$ can be found from the solution of

$$\nabla \cdot \vec{E}_0 = 0 = \nabla^2\psi_0 \tag{39}$$

Substitution of the free charge density and electric field in the charge conservation equation (Eq. (13)) yields

$$\begin{aligned}\frac{\partial \rho}{\partial t} + \nabla \cdot \left(\sigma \vec{E}\right) = \frac{\partial\left(\nabla\varepsilon \cdot \vec{E}_0 + \varepsilon\nabla \cdot \vec{E}_1\right)}{\partial t} \\ +\nabla \cdot \left(\sigma \vec{E}_0 + \sigma \vec{E}_1\right) = 0\end{aligned} \tag{40}$$

In AC electric field, the time-dependent electric field is presented in terms of a complex number. Thus, the charge conservation equation can be rewritten as

$$\begin{aligned}\left(\nabla\varepsilon \cdot \vec{E}_0 + \varepsilon\nabla \cdot \vec{E}_1\right) j\omega + \nabla\sigma \cdot \vec{E}_0 + \sigma\nabla \cdot \vec{E}_0 \\ +\nabla\sigma \cdot \vec{E}_1 + \sigma\nabla \cdot \vec{E}_1 = 0\end{aligned} \tag{41}$$

One can use the relationship presented in Eqs. (36a) to simplify the charge conservation equation as

$$\left(\nabla\varepsilon \cdot \vec{E}_0 + \varepsilon\nabla \cdot \vec{E}_1\right) j\omega + \nabla\sigma \cdot \vec{E}_0 + \sigma\nabla \cdot \vec{E}_1 = 0 \tag{42}$$

Finally, an equation for the divergence of perturbation electric field $\vec{E}_1$ can be obtained from the rearrangement of Eq. (42)

$$\nabla \cdot \vec{E}_1 = -\frac{\nabla\sigma \cdot \vec{E}_0 + \left(\nabla\varepsilon \cdot \vec{E}_0\right) j\omega}{\sigma + j\omega\varepsilon} \tag{43}$$

Substituting Eqs. (38) and (43) on Eq. (37) provides an expression for the AC electrothermal flow as

$$\vec{F} \cong \frac{(\sigma\nabla\varepsilon - \varepsilon\nabla\sigma) \cdot \vec{E}_0}{\sigma + j\omega\varepsilon}\vec{E}_0 - \frac{1}{2}\left|\vec{E}_0\right|^2 \nabla\varepsilon + (\rho - \rho_r)\vec{g} \tag{44}$$

The timescale for the fluid to response under an AC electric field is much slower than the applied electric field frequency. Thus, a time average forcing term can be applied to the flow equation. For the AC electrothermal flow, the time averaged electrical forcing term can be rewritten as

$$\begin{aligned}\left\langle \vec{F} \right\rangle \cong \frac{1}{2}\mathrm{Re}\left[\frac{(\sigma\,\nabla\varepsilon - \varepsilon\,\nabla\sigma) \cdot \vec{E}_0}{\sigma + j\omega\varepsilon}\vec{E}_0^*\right] \\ - \frac{1}{4}\left[\left(\vec{E}_0 \cdot \vec{E}_0^*\right)\nabla\varepsilon + (\rho - \rho_r)\vec{g}\right]\end{aligned} \tag{45}$$

The AC electrothermal flow can be obtained by solving Eqs. (30) and (31) with a time averaged forcing term given in Eq. (45). In case of the electrothermal process, the electric field for the forcing term can be obtained from the Eq. (39), with appropriate boundary conditions at the electrode. The electric field is applied on the metallic electrode surface. Under thin double layer assumption, the applied electric field can be connected with the bulk electrolyte potential by the charge conservation equation. In thin double layer, the lateral current due to advection or diffusion is much smaller than the normal current [35]. Thus, like ACEO process, the charge conservation can be expressed as a balance between charge storage rate in the double layer and the normal current as presented in Eq. (27), and the boundary condition for the electric potential can be deduced as [35]

$$\psi = V_e + \frac{\sigma}{i\omega C}\frac{\partial\psi}{\partial n}. \tag{46}$$

6.1 ACET pumping in microchip

The first known work on the electrothermal micro pumping was reported by Fuhr et al. in early 1990, where they observed the flow of low conductive distilled water in a microfabricated channel. In their work [28], a four-phase traveling wave electric field is used to drive fluids in which an array of electrodes (ten microns wide and ten microns gap) attained a peak velocity of ~180 μm s^{-1} at 35 V_{pp} and 100 kHz with fluid conductivity 9.3 mS m^{-1}. This demonstration showed practical possibilities of producing relatively high fluid velocity using a non-uniform electric field, which might be useful for micro pumping in the biomedical field. Sigurdson et al. [134] demonstrated the application of ACET effect to induce vortices in a pressure driven flow system to improve the binding rate of ligands in an assay. In their work, they have shown the transport of fluid in diffusion-limited reaction, where the binding rate factor is increased by seven when compared to conventional binding process. Later, Lian et al. [26] demonstrated AC electrothermal pumping of

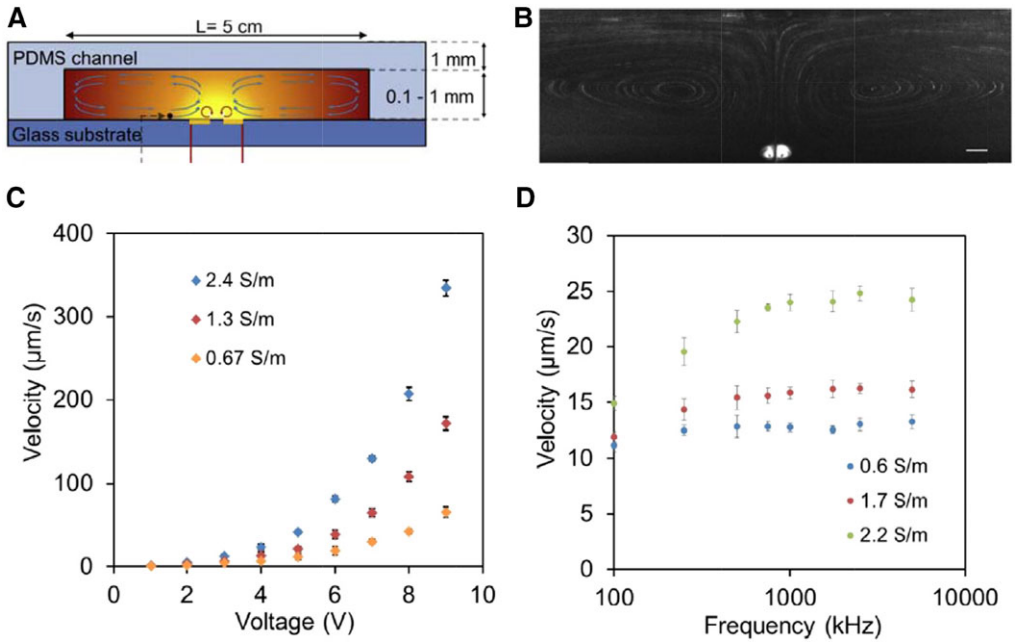

Figure 14. Long-range fluid motion induced by ACET. (A) A cross-sectional view of the microchannel integrated with a pair of parallel electrodes. Arrows indicate the direction of the flow. Black spots represent the location of velocity measurement. (B) Formation of two pairs of counter vortices in the microchannel. Fluorescence images were stacked together to illustrate the trajectories of the microspheres. Performance of the ACEO micropump at different (C) voltage and (D) applied electric field frequency. Reprinted from Lu et al. [41] (2016), with permission from Elsevier.

conductive liquids with an applied voltage level less than 25 V, and they claimed to achieve a local fluid velocity up to 80 μm/s. The same group also used a T-shaped electrode design to pump biofluid [135]. Using interdigitated coplanar electrodes, Koklu et al. [136] presented a parametric map for electrothermal vortices within the physiological conductivities considering the different size of channel heights.

Recently, Lu et al presented a design for long-range fluid motion induced by ACET [41]. Figure 14A shows the schematic of such a microdevice, where electrodes are formed on the bottom (glass substrate) layer, while the three other sides of the channel consist of PDMS. Their study has shown vortices that can span more than one centimeter (Fig 14B) if the channel height is in the order of a millimeter. On the other hand, smaller dimension microchannels (less than 300 microns) provide smaller counter vortices close to the electrode. They also developed a comprehensive computational model, which considers the buoyancy effects due to density gradient and temperature-dependent parameters. Their experimental results are in good agreement with numerical data if (i) buoyancy effect is considered, (ii) temperature dependent fluid properties are used, and (iii) a Robin type boundary condition is implemented for the temperature equation. Their extended numerical model also identified some major shortcomings of the general scaling law. For instance, their experimental data disagree with the claim that the local electrokinetic velocity is proportional to the fourth power of the applied voltage, especially for highly conductive biofluid. Loire et al. [137] also emphasized the role of buoyancy/natural convection forces on the electrothermal studies, which were predominantly ignored in many classical electrothermal theoretical works.

Since ACET takes place in a non-uniform AC electric field due to the conductivity gradient (spatial difference in conductivities) driven local temperature distribution resulted from the nonuniform Joule heating, a number of researchers tried to supplement the conductivity difference in the buffer furthermore using other innovative techniques. Perhaps, the most common choice to achieve this goal is to heat the microchannel and create an artificial temperature gradient [138]. Yuan and Wu [139] have demonstrated this thermally biased AC electrokinetic pumping by selectively heating one electrode, while maintaining the other electrode at room temperature. They have reported a significant improvement in the ACET flow velocity due to selective heating of one electrode, though their results were presented for very low applied electric potential. Recently, Williams and Green [140] presented the effect of external heating on the flow performance for AC electrothermal flow, where the heating elements were electrically isolated from the electrodes used for AC electric field. They have studied the effects electrode arrangement, size, and gap between electrodes using a numerical model.

Another innovative way to create the conductivity gradient is by strong illumination [141], microwave or laser heating. Green et al. [142] have shown the effect of light in the AC electrothermal flows by illuminating one electrode region, while keeping the other electrode at dark. They have noticed that the direction of fluid flow changes with frequency, though they still maintain counter-rotating vortices.

Later, they presented a self-similar solution to explain some of the experimental observations quantitatively [143]. Kwon and Wereley [141] have demonstrated rotationally symmetric vortices in light actuated electrothermal flow, where electrodes were formed on the top and bottom surfaces of a parallel plate microchannel; and conductivity gradient was enhanced by shining laser light on the top and bottom electrodes. Their study also emphasized the role of buoyant forces for the cases when the applied electric field frequency is above the charge relaxation frequency.

Conductivity difference in the buffer can also be created by maintaining a DC bias to AC signal on symmetric planar electrodes formed on the microchannel surface. Figure 15 shows the schematic of the negative and positive DC-bias AC electrothermal systems [144] used for pumping. In Fig. 15A, the right electrode is set as a net negative electrode, while the left electrode is as a net positive. Due to electrochemical reactions at the electrode-electrolyte interface (aka Faradic reactions), co-ions are produced and released on the electrolytes. Thus, for the negative DC-bias case, cations are produced on the net positive (left) electrode, while anions are gathered on the right electrodes as seen from Fig. 15A. These anions and cations are responsible for setting up different pH – acidic on the cationic side and basic on the anionic side.

Ng et al. [144] reported the formation of acidic and basic domain due to the release of ions from the electrodes, and these additional ions alter the conductivity of the solution. For instance, from their experimental work, high conductivity is observed for the net negative electrode and low conductivity

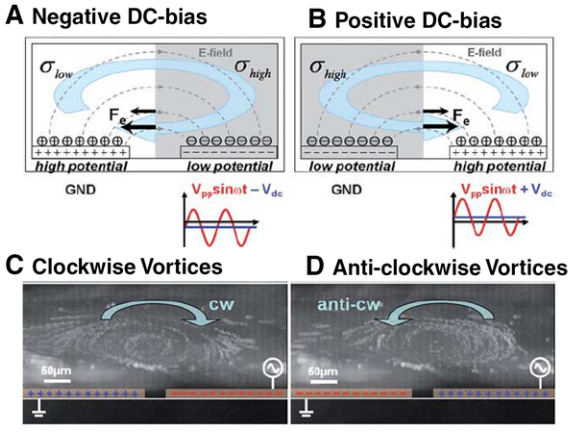

Figure 15. Schematic and working principle of DC bias AC electrothermal flow for (A) negative and (B) positive bias. Experimental results of fluid flow close to the electrode regions for (C) negative DC bias (-1.5 V_{DC}) AC voltage (10 V_{PP} and 100 kHz) and (D) positive DC bias (+1.5 V_{DC}) AC voltage (10 V_{PP} and 100 kHz). Here the microchannel is 5 mm wide and 200 microns high. Each electrode is 1 mm wide and there is 20 microns gap between them. DC bias AC electrothermal flow can be applied to obtain higher flow strength than the regular AC electrothermal flow, where the direction of vortices can be modulated by the polarity of the bias potential. Reproduced from Ng et al. [144] with permission of the Royal Society of Chemistry.

are found for the net positive electrode, causing a conductivity gradient along the channel. Under the action of an AC electric field, fluid is moved from the higher conductivity region to the lower one creating clock-wise vortices next to electrodes. Similarly, in Fig. 15B, the electrode setting is just opposite of the Fig. 15A, and anti-clockwise fluid vortices are obtained as shown in Fig. 15D.

Like ACEO flow cases [145], asymmetrical electrode configurations were also explored in ACET flow. Vafaie et al. [146] presented so-called discretized electrodes for forward and backward pumping using asymmetric electrode configurations and switching of electrodes for positive and negative potentials. Asymmetrical electrodes configuration is used to create AC electrothermal flow to improve the binding reaction efficacy in a microchannel immunoassay [147]. Wu et al. [148], demonstrated the ACET flow driven vortex in a micromixer, where the fluid flow is created by 3D electrodes imprinted on the channel side wall. Salari et al. [149] developed an electrothermal micropump by placing asymmetrical electrodes on all sides of the microchannel. Lang et al. [150] used thirty pairs of asymmetrical electrode arrays to develop a close loop electrothermal micropump to grow human embryonic kidney cells and human colon carcinoma cells in a microfluidic chip.

Although there is a significant interest in AC electric field driven fluid motion in microdevices using ACEO and/or ACET, none of these methods were able to create a pressure gradient for a sustained net flow like DC electroosmotic pumps. Also, working with ACET for high conductivity fluids is not very desirable for the biological sample as excessive temperature rise happens in highly conductive biofluid especially close to the electrode, which may damage the biological activities of samples. Thus, extreme care must be taken to adopt this technology for highly conductive biological buffers or proteins.

7 Induced charge electroosmosis (ICEO)

When an electric field (AC or DC) is applied to a polarizable post or an object embedded in an electrolyte, a dipolar charge is induced leading to the formation of a dipolar double layer as shown in Fig. 16B [30]. Due to the formation of the dipolar double layer, the applied electric field becomes tangent to the surface of the post or object, and causes an electroosmotic flow which is known as induced charge electroosmotic (ICEO) flow (Figs. 16C & D) [33]. ICEO flow is observed both around the neutral polarizable object as well as the charged polarizable object [151–153]. ICEO phenomena are especially important at the smaller zeta potential [30]. Bazant and Squires demonstrated that when total zeta potential (initial + induced) ζ is much smaller than $2(kT/e)\log(L/\lambda_D)$, ICEO dominates over other electrokinetic effects. Otherwise, nonequilibrium electrosurface phenomena (NESP), second kind electrokinetic phenomena etc. dominates [154–156].

Like DC and AC electroosmosis, induced charge electroosmosis (ICEO) is a consequence of the interaction between the electric field and electric double layer. However, ICEO is different from other electroosmosis due to the nature and formation of the double layer from the surface electric conditions. In regular fixed charge or classical DC electroosmosis, zeta potential remains uniform throughout the material as an equilibrium surface property. In contrast, the zeta potential is induced in ICEO by the applied electric field due to charge accumulation, which is non-uniform and dipolar in nature. Squires and Bazant [30] provided the detailed theoretical analysis of ICEO for various conditions based on the thin double layer ($\lambda_D << r_0$) and weak applied electric field ($E_0 r << k_B T/ze$) approximation. In the following section, we briefly reviewed their theoretical model.

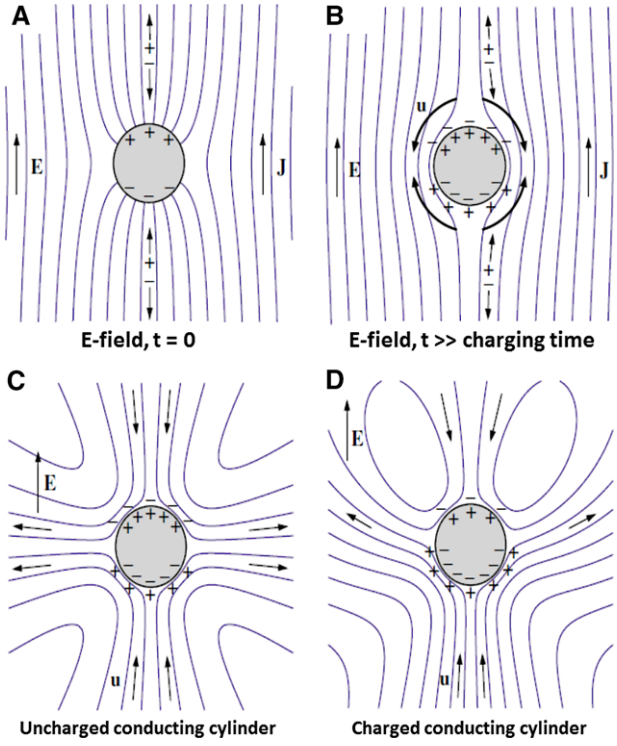

Figure 16. Induced-charge electroosmosis phenomena around a metal cylinder in a binary electrolyte; (A) sudden application of electric field, t = 0 initiates polarization where electric field lines are perpendicular to the surface. Application of electric field facilitates electric current, J which drives opposite ions around the cylinder on the two sides. (B) After charging time, dipolar double layer forms at the two-opposite side of the cylinder. This dipolar double layer acts like an insulator and electric field lines become tangential around the cylinder. (C) The tangential electric field exerts a force on the accumulated charges on the dipolar double layer and causes electroosmotic flow around the conducting cylinder with zero net charges. (D) Similar dipolar double layer and electroosmotic flow are observed for the charged conducting cylinder. However, dipolar double layer formation for a charged particle is unbalanced and double layer on one side of the cylinder dominates over the double layer on the other side. Hence, resultant electroosmotic flow is asymmetric, which causes a streaming flow in the upward direction. Reprinted this figure with permission from Bazant and Squires [30]. Copyright (2004) by the American Physical Society.

When an electric field ($E_0\hat{k}$) is applied to an uncharged conductive cylinder of radius r_0 immersed in an electrolyte solution (Fig. 16A), the electric field lines intersect at a right angle on the cylinder and form an equipotential surface with an electric potential of φ_0, which is given by [33]:

$$\varphi_0 = -E_0\left(1 - \frac{r_0^2}{r^2}\right) \tag{47}$$

In the absence of electrochemical reaction, ions in the electrolytes move toward the cylinder and form dipolar screening of ion clouds around the cylinder surface. The formation of screening ion cloud facilitates a time-dependent induced zeta potential around the cylinder surface. The time-dependent zeta potential can be obtained from surface charge density (q), applied electric field and electrolyte conductivity (σ) as given by [30]

$$\frac{d\zeta(\theta)}{dt} = \frac{\frac{dq(\theta)}{dt}}{\varepsilon\kappa} = \frac{\sigma}{\varepsilon\kappa}\vec{E}\cdot\hat{r} \tag{48}$$

where ε is the permittivity of the electrolyte solution, $\kappa^{-1} = \lambda_D$ is the Debye screening length and $\hat{r}$ is the unit vector in the radial direction. The system eventually reaches to steady state configuration when the formation of the dipolar double layer around the cylinder is complete and expels all electric field lines i.e. electric field lines become tangent around the cylinder surface ion-cloud, leaving no normal component as shown in Fig. 16B. The tangential component of electric field is obtained as follows

$$E_t = \hat{\theta}\cdot\vec{E} = -2E_0\sin\theta \tag{49}$$

At this configuration, the electric potential outside the screening cloud can be expressed as

$$\varphi_0 = -E_0\left(1 + \frac{r_0^2}{r^2}\right) \tag{50}$$

Thus, the spatially non-uniform zeta potential around the surface can be obtained as follows [30]

$$\zeta(\theta) = \varphi_0 - \varphi_f(\theta) = 2E_0 r_0\cos\theta \tag{51}$$

The tangential component of applied electric field acts on the EDL formed by the non-uniform zeta potential and causes induced charge electroosmotic flow (ICEO). The ICEO slip velocity around this cylinder is found from classical Helmholtz-Smoluchowski formula as follows

$$\begin{aligned}\vec{u}_{ICEO} &= -\frac{\varepsilon_w\zeta}{\mu}E_t\hat{\theta} = -\frac{\varepsilon_w 2E_0 r_0\cos\theta}{\mu}(-2E_0\sin\theta)\hat{\theta} \\ &= 2U_0\sin 2\theta\hat{\theta}\end{aligned} \tag{52}$$

where U_0 is the order of velocity scale for ICEO, which can be presented as

$$U_0 = \frac{\varepsilon_w E_0^2 r_0}{\mu} \tag{53}$$

ICEO velocity is stronger than regular electroosmosis since it depends on the square of the applied electric field. For a charged cylinder as shown in Fig. 16D, i.e. cylinder with

a non-zero equilibrium charge density, $q_0 = \frac{Q}{4\pi r_0^2}$, the steady state zeta potential distribution has both constant uniform zeta potential and induced non-uniform potential as follows

$$\zeta(\theta) = \zeta_0 + 2E_0 r_0 \cos\theta \tag{54}$$

Hence, the ICEO slip velocity for a charged cylinder will be a superposition of slip velocity due to constant equilibrium zeta potential and slip velocity due to induced non-uniform zeta potential as shown in Eq. (52) as given by [30]

$$\vec{u}_{ICEO}^{Charged} = \vec{u}_s - 2\frac{\varepsilon_w \zeta_0 \sin\theta}{\mu}\hat{\theta} \tag{55}$$

For time-dependent ICEO, the slip velocity for charged or uncharged cylinder, Janus particles, insulating or conducting post can be found in [30,157–159]. ICEO can also be obtained in an AC electric field. The governing equations for ICEO include Maxwell's equation, charge conservation equation (Eq. (15)) and fluid flow equation (Eqs. (16) and (17)). For typical microfluidic ICEO, the Navier Stokes equations reduce to Stokes equations because of the assumption mentioned in ACEO section.

7.1 ICEO as pumping mechanism

At the early stage of theoretical development of ICEO phenomena, the primary focus was on the flows around polarizable cylindrical posts in a uniform electric field where a quadrupolar flow can be obtained as seen in Fig. 16. Later, Bazant and Squires demonstrated that the ICEO can be used to drive fluid flow in any direction by designing and breaking the spatial symmetry of conducting posts relative to the background AC or DC electric field [159]. The spatial symmetry on the conducting post can be broken by dielectric or conductive coating or by optimizing the shape and topology of the posts to control ICEO flow [158, 160, 161].

Squires and co-workers demonstrated ICEO micropumps using arrays of Janus metallo-dielectric micropillars [162]. Unidirectional ICEO flow is obtained upon application of AC electric field across the channel length by breaking symmetry with the Janus micropillars. The schematic of the micropillars array, as well as other control mechanisms used in their study, are shown in Fig. 17A–D. The microfluidic ICEO pump was tested with seven different electrolytes (two strong and five weak electrolytes) solutions, and the pK values of solution were varied by varying buffer composition for evaluating the effect on the ICEO velocities. The operating applied AC potential on the driving electrodes was varied between 100 and 175 V_{PP} and frequencies between 1 and 20 kHz. Fluid velocities, measured using microPIV, were observed on the low-pressure side of the channel loop. The pump pressure was measured for various combinations of electric field strengths and frequencies as well as electrolytes as shown in the Fig. 17G. The lowest pressure was found to be 15 Pa for 100 μM KCl and the highest pressure was 150 Pa for 100 μM Tris buffer. They have reported that the pump pressure varies with applied potential as $\Delta p \propto \phi^{0-2}$ depending on the frequency, type of electrolyte and applied voltage.

Breaking symmetries of ICEO flow through irregular shaped posts, non-uniform surface properties, controlled potential and field gradients etc. are the key to producing streaming flow in this type of micropump [158, 159]. Recently it is reported that ICEO flow increases with the increasing concentration of NaCl and KCl [163], but it was previously considered that the ICEO velocity decays with increasing concentration in general [157, 164]. ICEO pumping velocity and mass flow rate are also dependent on the size and relative orientation of circular posts [165, 166]. Gregerson et al. [158] developed a mathematical model for shape and topology optimization to improve the pumping capability of ICEO micropumps.

8 Dielectrophoresis

Dielectrophoresis (DEP) is widely used for movement of polarizable particles in fluid media under the action of a nonuniform electric field [167]. DEP mechanism is classified based on the nature of the electric field, such as AC DEP, DC DEP, traveling wave DEP etc. Depending on magnitude and direction of the applied electric field, dielectrophoretic force can create movement of particles in a preferred direction. In a densely populated particulate system, the particle movement can cause a fluid flow and it is reported to use as a pumping mechanism in microfluidics [168, 169]. The various mechanisms for DEP based fluid pumping are described in the following sections.

8.1 Traveling wave dielectrophoresis (twDEP)

Traveling wave DEP is created for movement of particles in a preferred direction by imposing phase differences in the applied AC electric potential on electrode surfaces. Like ACEO or ACET, planar electrodes are used for the creation of AC electric field, but the phase difference between consecutive electrodes are not set at 180°. Figure 18 shows a schematic of a traveling wave DEP system, where continuous phase differences in the applied AC electric potential is achieved through a series of microelectrodes. The delay in phase differences at different electrodes creates a moving electric field gradient which either attracts suspended particles in the direction of propagation or drives away particles in opposite direction of electric field propagation. The movement of sufficiently dense particles induces flow and entire fluid domain moves in the same direction of particles motion [28].

In case of an electric field driven particulate flow, the time scale of particle motion is usually much smaller than that of the electric field. Hence the electrostatic potential distribution for particulate flow is obtained from the quasi-electrostatic model. In the quasi-electrostatic model, the Maxwell's equations can be reduced to Eqs. (8)–(10).

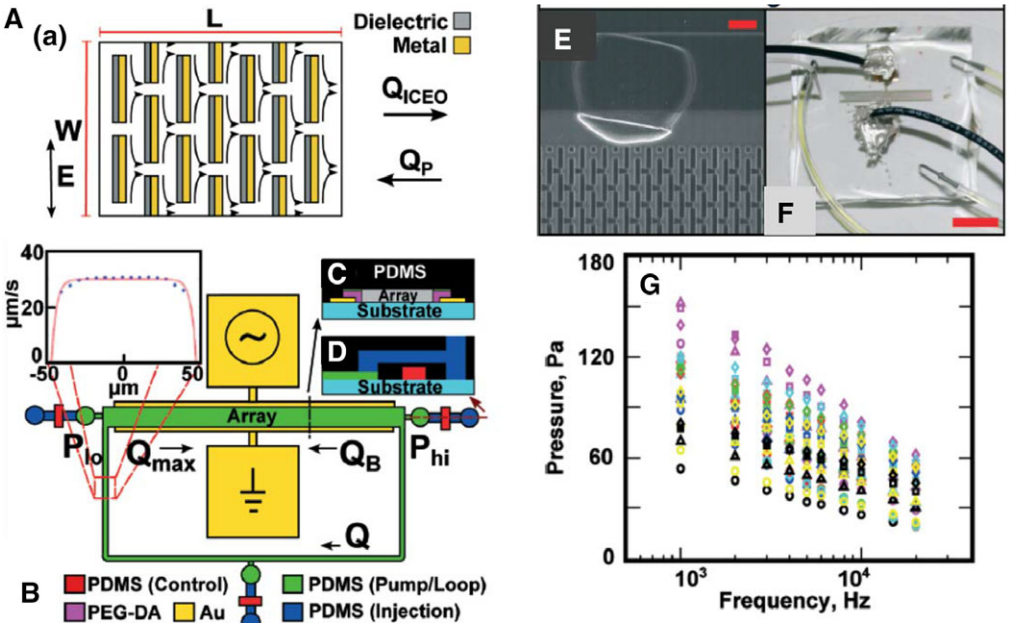

Figure 17. (A) Schematic of ICEO pumping mechanism using an array of metallo-dielectric Janus micro-pillars. The applied AC electric field in vertical direction drives ICEO flow, Q_{ICEO} from left to right. (B) Microfluidic channel for ICEO flow in a loop. The velocity profile was constructed from the microPIV measurement. (C) Side view of array region in the microfluidic ICEO pump. (D) A sectional view of multilayer microchannels at the inlet. (E) SEM image of array region showing electrically permeable hydrogel plugs along the driving electrodes for blocking backflow (scale bar 50 μm). (F) Picture of a complete working ICEO pumping device (scale bar 1 cm). (G) ICEO pump pressure measured for ten frequencies between 1 and 20 kHz, four different voltages (100 Vpp, circles; 125 Vpp, triangles; 150 Vpp, squares; 175 Vpp diamonds), and seven electrolytes (KCl, black; NaCl, blue; chloroacetate, pKa 2.9, yellow; acetate, pKa 4.8, cyan; MES, pKa 6.2, green; MOPS, pKa 7.2, red; Tris, pKa 8.3, magenta). Reproduced from Paustian et al. 2014 with permission of the Royal Society of Chemistry.

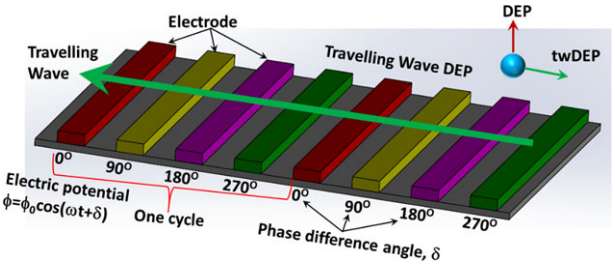

Figure 18. Schematic representation of an array of microelectrodes for traveling wave DEP. Travelling waves are created by using phase difference of π/2 between the electrodes. Traveling wave DEP facilitates electrostatic force parallel to the direction of wave propagation in addition to the conventional vertical force. The phase difference creates spatial variation in the electric field which provides a movement of the suspended particles in the fluid media. Hence, it creates unidirectional flow of particles and an induced fluid motions in the microchannel.

In pure DEP, charges are the major current carriers and the effects of ionic current are negligible. For a linear, isotropic and homogeneous medium, the current density due to the inherent carrier can be given as $\vec{J} = \sigma \vec{E}$, and the charge conservation equation (Eq. (13)), can be rewritten as

$$\frac{\partial \rho_e}{\partial t} + \nabla \cdot \left(\sigma \vec{E}\right) = 0 \tag{56}$$

Now, the time derivative of Eq. (11) and a complex variable presentation of electric potential $\tilde{\psi}(\vec{r}, t) = \psi_0(\vec{r})\, e^{j\omega t}$ yield

$$\frac{\partial \rho_e}{\partial t} = -\nabla \cdot \frac{\partial}{\partial t}\left(\varepsilon \nabla \tilde{\psi}\right) = -j\omega \nabla \cdot \left(\varepsilon \nabla \tilde{\psi}\right) = j\omega \rho_e \tag{57}$$

Substitution of Eq. (57) in Eq. (56) gives

$$j\omega \rho_e + \nabla \cdot \left(\sigma \vec{\tilde{E}}\right) = j\omega \nabla \cdot \left(\varepsilon \vec{\tilde{E}}\right) + \nabla \cdot \left(\sigma \vec{\tilde{E}}\right) \tag{58}$$

Alternatively, the above equation can be written as

$$\nabla \cdot \left(j\omega \varepsilon \vec{\tilde{E}} + \sigma \vec{\tilde{E}}\right) = \nabla \cdot \left(\tilde{\varepsilon} \nabla \tilde{\psi}\right) = 0 \tag{59}$$

where the complex permittivity can be given as $\tilde{\varepsilon} = \varepsilon + \frac{\sigma}{j\omega} = \varepsilon - j\frac{\sigma}{\omega}$.

The electric potential distribution for twDEP is obtained by solving Eq. (59) for both fluid and particle domain. This requires proper boundary conditions as well as interface conditions between particle and fluid interface. The typical boundary conditions are as follows:

$$\tilde{\phi}(\vec{x}) = \phi_0 e^{j(\omega t + \delta)} \rightarrow \text{on an electrode surface} \tag{60}$$

$$\frac{\partial \tilde{\phi}(\vec{x})}{\partial \vec{x}} = 0 \rightarrow \text{on an insulating surface} \tag{61}$$

The continuity of the electric potential and the normal component of the electric flux density are imposed as interface conditions between particle and fluid interface as:

$$\tilde{\phi}_p = \tilde{\phi}_f \tag{62}$$

$$\tilde{\varepsilon}_p \frac{\partial \tilde{\phi}_p}{\partial \vec{n}} = \tilde{\varepsilon}_f \frac{\partial \tilde{\phi}_f}{\partial \vec{n}} \tag{63}$$

where the subscript p is for the particles, f is for the fluid media and $\vec{n}$ is the surface normal. The volumetric dielectrophoretic force is calculated from the time-averaged Maxwell stress tensor by integration over the period of the AC electric potential. Hence the time-averaged dielectrophoretic force density on the particle surface can be given by [170]

$$\begin{aligned} F_{DEP} &= \vec{\vec{M}}_M\Big|_{TA} \cdot \vec{n} = \left(\frac{1}{T}\int_0^T \vec{\vec{M}}_M dt\right) \cdot \vec{n} \\ &= \frac{1}{4}\mathrm{Re}(\tilde{\varepsilon})\left[(\tilde{\vec{\vec{E}}}\,\tilde{\vec{\vec{E}}}^{*} + \tilde{\vec{\vec{E}}}^{*}\,\tilde{\vec{\vec{E}}}) - \left|\tilde{\vec{\vec{E}}}\right|^2 \vec{\vec{I}}\right] \cdot \vec{n} \end{aligned} \tag{64}$$

where $\tilde{\vec{\vec{E}}}^{*}$ is the conjugate of $\tilde{\vec{\vec{E}}}$, $\vec{\vec{I}}$ is the unit tensor, $\tilde{\vec{\vec{E}}}\,\tilde{\vec{\vec{E}}}^{*}$ is the dyadic product of electric field and its conjugate.

Although Maxwell stress tensor-based estimation of DEP force is considered as the most accurate method, it requires the solution of complex electric potential ($\tilde{\psi}(\vec{r}, t)$) in a fluid domain embedded with particles or posts. The computational process of Eq. (59) is very challenging and it requires interface-resolved sophisticated numerical methods with high computational cost [36, 171]. Fortunately, there exists an alternative approach to evaluate DEP force based on the effective dipole moment method. In this method, particles are considered as point charges and the effect of polarization is accounted through the dipole moment. In this simplified case, the electric potential distribution is estimated by solving Laplace equation (Eq. (39)) in the fluid domain without considering the presence of particles. Wang et al. [172] presented a unified effective dipole moment based force expression as

$$\begin{aligned} \vec{F}_{g\,DEP}(\vec{r}, t) &= \left[\vec{p}(\vec{r}, t) \cdot \nabla\right] \tilde{\vec{\vec{E}}}(\vec{r}, t) \\ &= \left[p_x(t)\tfrac{\partial}{\partial x} + p_y(t)\tfrac{\partial}{\partial y} + p_z(t)\tfrac{\partial}{\partial z}\right] \tilde{\vec{\vec{E}}}(\vec{r}, t) \end{aligned} \tag{65}$$

where $\vec{p}(\vec{r}, t)$ is the induced dipole moment, p_x, p_y and p_z are components of induced dipole moment in x, y and z-direction of Cartesian coordinate, and the AC electric field can be expressed as

$$\tilde{\vec{\vec{E}}}(\vec{r}, t) = \mathrm{Re}(\vec{\vec{E}}_0(\vec{x})e^{j(\omega t+\delta)}) = E_x(t)\hat{i} + E_y(t)\hat{j} + E_z(t)\hat{k} \tag{66}$$

where $\hat{i}$, $\hat{j}$, $\hat{k}$ are the unit vector in Cartesian x, y, z coordinates, respectively, $E_x(t) = E_{0x}(x, y, z)\cos[\omega t + \delta_x(x, y, z)]$, $E_y(t) = E_{0y}(x, y, z)\cos[\omega t + \delta_y(x, y, z)]$, $E_z(t) = E_{0z}(x, y, z)\cos[\omega t + \delta_z(x, y, z)]$ and E_{0x}, E_{0y}, E_{0z} are the magnitudes of the electric field, δ_x, δ_y, δ_z are the phases of electric potential in x, y, z direction. Using superposition principle, Huang et al. [173] derived an expression for dipole moment as follows

$$\vec{p}(\vec{r}, t) = 4\pi\varepsilon_f r^3 \begin{bmatrix} E_{0x}\left\{\mathrm{Re}[\chi_{CM}]\cos(\omega t+\delta_x) - \mathrm{Im}[\chi_{CM}]\sin(\omega t+\delta_x)\right\}\hat{i} \\ +E_{0y}\left\{\mathrm{Re}[\chi_{CM}]\cos(\omega t+\delta_y) - \mathrm{Im}[\chi_{CM}]\sin(\omega t+\delta_y)\right\}\hat{j} \\ +E_{0z}\left\{\mathrm{Re}[\chi_{CM}]\cos(\omega t+\delta_z) - \mathrm{Im}[\chi_{CM}]\sin(\omega t+\delta_z)\right\}\hat{k} \end{bmatrix} \tag{67}$$

where $\chi_{CM} = (\tilde{\varepsilon}_p - \tilde{\varepsilon}_f)/(\tilde{\varepsilon}_p + 2\tilde{\varepsilon}_f)$ is the Clausius-Mossotti factor. Since typical AC frequencies in DEP is below 100 MHz, it satisfies quasi-electrostatic approximation. Hence $\frac{\partial E_x(t)}{\partial y} = -\frac{\partial^2 \phi}{\partial y \partial x} = -\frac{\partial^2 \phi}{\partial x \partial y} = \frac{\partial E_y(t)}{\partial x}$ and using Eqs. (65) and (67), the generalized DEP force in the x-direction is given by [173]

$$\begin{aligned} F_{g\,DEP,x} = p_x(t)\tfrac{\partial}{\partial x}E_x(t) = 4\pi\varepsilon_f r^3 E_{0x}\big[&\mathrm{Re}[\chi_{CM}]\cos(\omega t + \delta_x) \\ &-\mathrm{Im}[\chi_{CM}]\sin(\omega t + \delta_x)\big] \\ &\big[\tfrac{\partial E_{0x}}{\partial x}\cos(\omega t + \delta_x) - \tfrac{\partial \psi_x}{\partial x}\sin(\omega t + \delta_x)\big] \end{aligned} \tag{68}$$

The time-averaged generalized DEP force component in x-direction is obtained from above equation as follows

$$F_{g\,DEP,x} = 2\pi\varepsilon_f r^3 \left(\mathrm{Re}[\chi_{CM}]E_{0x}\frac{\partial E_{0x}}{\partial x} + \mathrm{Im}[\chi_{CM}]E_{0x}^2\frac{\partial \delta_x}{\partial x}\right) \tag{69}$$

Similarly, the time-averaged component of generalized DEP force in y and z-direction can be obtained. The effective dipole moment based generalized DEP equation is given by [172]:

$$\begin{aligned} \vec{F}_{g\,DEP} = 2\pi\mathrm{Re}(\tilde{\varepsilon}_f)\, r^3 \big[&\mathrm{Re}\,(\chi_{CM})\nabla E_{rms}^2 + \mathrm{Im}(\chi_{CM}) \\ &(E_x^2\nabla\delta_x + E_y^2\nabla\delta_y + E_z^2\nabla\delta_z)\big] \end{aligned} \tag{70}$$

where the first term represents the spatial nonuniformity of applied electric field which is relevant to the conventional DEP force, and the second term represents spatial phase distribution to account the effect of the traveling wave. The second term goes to zero for conventional DEP since the electric field is phase independent.

The particles move toward the positive gradient of the electric field when $\mathrm{Re}\,(\chi_{CM})$is positive and vice versa. On the other hand, the particles move along the propagating direction of the traveling wave when $\mathrm{Im}(\chi_{CM})$ is positive and against the propagating direction of the traveling wave when $\mathrm{Im}(\chi_{CM})$ is negative. The maximum effect of twDEP is observed near the Maxwell-Wagner relaxation frequency,

$$f_{M-W} = \frac{1}{2\pi}\left(\frac{\sigma_p + 2\sigma_m}{\varepsilon_p + 2\varepsilon_m}\right) \tag{71}$$

8.1.1 Traveling wave DEP for microfluidic pumping

Unlike a fixed electric field minima or maxima in conventional DEP, traveling wave DEP creates a moving point of attractions i.e. moving electric field minima or maxima for particles so that particles can be continuously transported in a certain direction. The second term of Eq. (70) should be large enough so that it can overcome fluid drag force as well as a component of the first term of Eq. (70) which acts against this (second) forcing term [174]. These forces can be optimized for a continuous flow by regulating the electrical properties of fluids and suspended particles, applied electric field strength, and frequencies (see Table 2).

Lei et al. [177] demonstrated microfluidic blood delivery using the twDEP pump, where an array of microelectrodes is deposited at the bottom of the glass-PDMS rectangular

Table 2. Comparisons of various travelling wave dielectrophoretic pumping

Author and year	Velocity	Applied voltage	Pumping fluid
Fuhr et al. [28]	190 μm/s	35 V	Aqueous solution with suspended latex microparticles
Hagedorn et al. [29]	600 μm/s	12 V	Water with suspended microsphere
Masuda et al. 1988	10 μm/s	1.5 V	Sucrose solution with suspended erythrocytes
Pethig et al. [175]	64 μm/s	1.06 V_{rms}	Monocytes cells suspending in glucose, sucrose solution
Tseng et al. [176]	25 μm/s	5.5 V	Red blood cells suspending in glucose, sucrose solution
Wang et al. [177]	4.2 μm/s	2 V	Red blood cells suspending in glucose, sucrose solution
Lei et al. [178]	15 μm/s	15 V	Red blood drops

microchannel. They applied an AC potential (3 to 5 V) with a frequency range from 1 to 40 MHz and phase shift of 90 or 120° between neighboring electrodes (repeats in every 4th electrodes) to create a significant variation of conventional and traveling wave DEP forces.

Figure 19A shows the variation of non-dimensional conventional and traveling wave DEP forces at the half of the channel depth. The twDEP forces are positive in the region of electrodes and decay rapidly beyond the electrode regions. On the other hand, the conventional DEP force is weaker in the electrode region and stronger near the reservoir. This observation is in line with the previous experimental findings of Hughes [178] where it was reported that the conventional DEP force is higher than the twDEP force within 5 μm of the reservoir. Near the reservoir, the conventional DEP force works against the twDEP force. However, because of the stronger twDEP force over electrode region, blood cells are pushed forward and a lower pressure is created at the upstream compared to the downstream region. The motion of blood cells causes a continuous flow, and the flow velocity was measured using microscale particle image velocimetry – microPIV. The velocity of cell within the microchannel is shown in Figs. 19B –D as a function of applied frequency and number of electrodes, respectively.

Their experiment reveals that the velocity increases as the peak to peak applied voltage increases (not shown here). They have reported a minimum peak to peak voltage of 3 V for pumping, and blood cells were damaged at 6 V. There is an optimum frequency for which the pumping velocity reaches its maximum depending on the phase lag. For their experiment, the optimum frequency is 20 and 30 MHz for a phase difference of 90 and 120°, respectively. It is also reported that the average velocity increases with the increase in the number of electrodes due to stronger twDEP force.

Application of traveling wave electric field can also facilitate other types of electrohydrodynamic pumping [179]. He and Liu [180] presented the effect of electrohydrodynamics on twDEP pumping. Recently, multifluid mixing and pumping [181], modulation of blood flow in microchannels [176], separation and transportation of cells etc. are demonstrated where twDEP is used as a primary fluid driving mechanism [182, 183]. Tseng et al. [175] designed and developed a driving circuit that can efficiently replace function generator for steady state twDEP pumping of the blood sample in a microchannel.

8.2 Liquid dielectrophoresis (LDEP)

Liquid dielectrophoresis (LDEP) is defined as the motion of the liquid in an air-liquid interface or bubble within a liquid due to the application of a non-uniform AC or DC electric field [184, 185]. The fundamental working principle of LDEP is shown in Fig. 20. When a non-uniform electric field is applied in a liquid-air interface or liquid-bubble mixture, polarization takes place. In case of a liquid-air interface (Fig 20A), dielectric liquid is drawn to the higher intensity electric field since it is more polarizable than the gas. On the other hand, for the liquid-bubble mixture (Fig. 20B), gas or vapor bubbles are driven away from higher intensity electric field. Like ACET, LDEP is distinct from many electrokinetic mechanisms, where flows are primarily originated from the ion-drag effect or electroconvection.

There are some similarities between LDEP and electrowetting as LDEP can be used to move liquid from a droplet using a pair of electrodes. However, unlike electrowetting, in LDEP the electric field lines penetrate through the liquid and control the shape of the liquid front that moves between electrodes [186]. Usually, the contact angle of LDEP is higher than the electrowetting. LDEP can be used to move conductive liquid too using an AC current. In case of conductive liquid, the microelectrodes have to be coated with a very thin dielectric layer and liquid pumping depends on the applied frequency of AC electric field and the thickness of dielectric layer [186]. If the applied frequency is greater than the crossover frequency, the conductive liquid behaves like a dielectric liquid, and in that case, the conductive fluid is driven like a moving finger front. On the other hand, conductive fluid cannot be moved using a frequency lower than the crossover frequency. In that case, fluid just spreads on the substrate as shown in Fig. 21C.

If a liquid is placed between two energized electrodes as shown in Fig. 21A, the electric field induced force acts on the interface between liquid and gas to facilitate motion of the liquid. This interfacial force is found from Kelvin-Helmholtz formulation [45, 187] as follows:

$$\vec{F} = \rho_f \vec{E} - \frac{1}{2}\left|\vec{E}\right|^2 \nabla\varepsilon + \nabla\left(\frac{1}{2}\left|\vec{E}\right|^2 \rho\, \partial\varepsilon/\partial\rho\right) \tag{72}$$

The similar formulation is obtained from Maxwell stress tensor as discussed for Eq. (19). For an uncharged and incompressible liquid, the first and the last term of right-hand

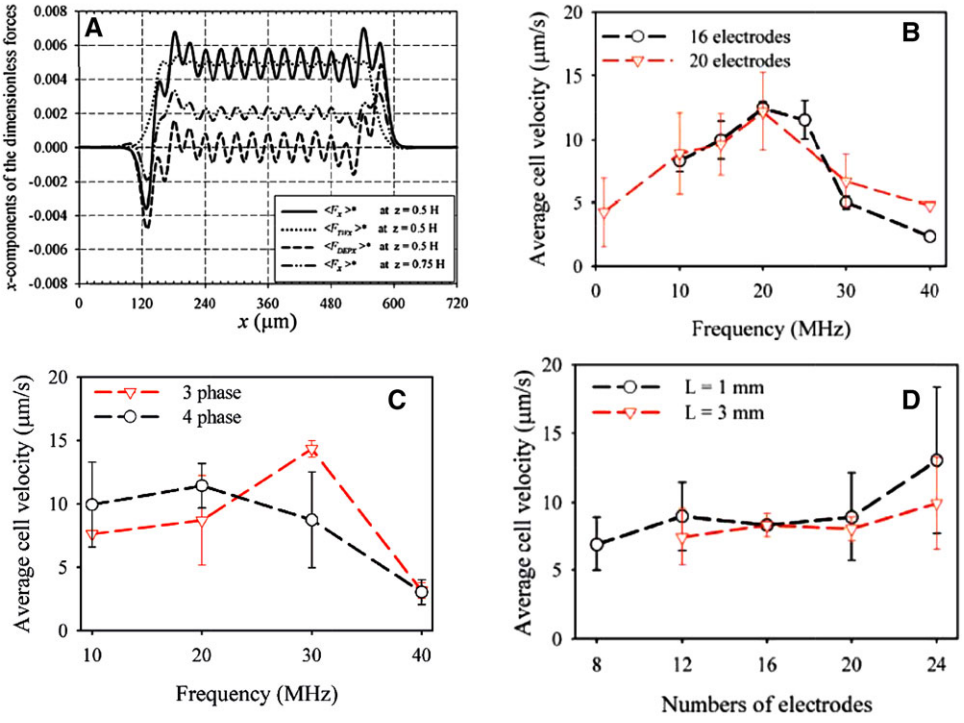

Figure 19. Performance of a traveling wave dielectrophoretic pump for human blood delivery. (A) Distribution of dimensionless conventional DEP and twDEP forces along the channel length. Average cell velocities as a function of (B) applied frequencies, (C) number of phases and (D) number of electrodes. Reproduced from Lei et al. [177] with copyright permission of the Royal Society of Chemistry.

side of the forcing equation can be neglected. At the interface, the DEP force (the second term in the Eq. (72)) can create a hydrostatic pressure difference between liquid and gas, which is similar to capillary force at the curved surface [184]. Thus, the hydrostatic pressure difference at the interface can be obtained [184] as

$$p_{liquid} - p_{air} = \frac{1}{2} E_t^2 \left(\varepsilon_{liquid} - \varepsilon_{air}\right) \tag{73}$$

However, strictly speaking, the LDEP is not a pumping mechanism. Nevertheless, it can provide a flow of liquid or bubbles in a way similar to the fluid flow in the capillary tube through capillary action or surface tension. In LDEP literature, the height rise of the liquid between narrowly

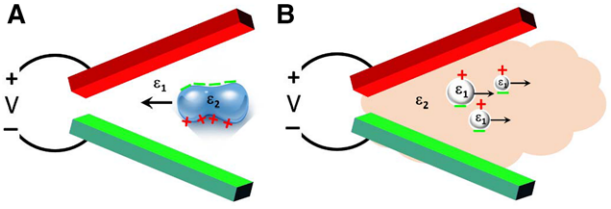

Figure 20. Schematic of liquid dielectrophoretic actuation; (A) dielectric liquid (ε_2) is in contact with air (ε_1 and $\varepsilon_1 < \varepsilon_2$) are placed between two electrodes. Upon activation of electrodes, the liquid-air system polarizes and dielectric liquid is drawn into stronger electric field region, which is on the convergent side of the electrode system. (B) When a dielectric liquid (ε_2) with bubbles (ε_1) is placed between energized electrodes, the bubbles are driven away from the stronger electric field region (the divergent section) due to the lower dielectric permittivity of the bubble.

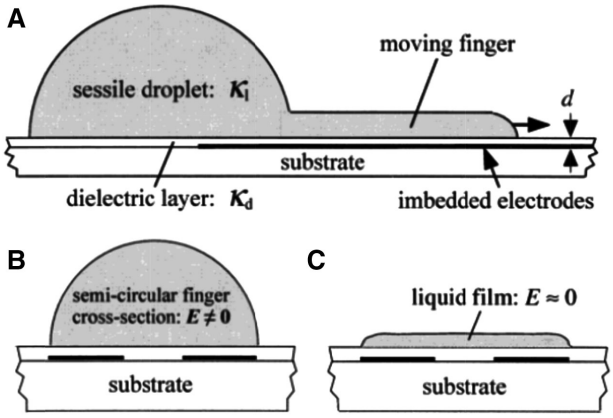

Figure 21. The effect of applied electric field frequency on DEP liquid manipulation. (A) Dielectrophoresis actuated liquid flow as a moving finger from the droplet towards the other end of the electrodes, (B) cross-section of the water finger showing semicircular profile when $f >> f_c$, (C) cross-section of slowly spreading water film when $f << f_c$. In Figure (C), the electric field lines cannot penetrate the liquid. Reprinted with permission from Jones [186]. Copyright (2002) American Chemical Society.

spaced electrodes is calculated based on Pellet's classical experiment [188] as

$$h \approx \frac{\left(\varepsilon_{liquid} - \varepsilon_{air}\right)\left|\vec{E}\right|^2}{2\rho_l g} \tag{74}$$

The liquid dielectrophoretic pumping mechanism is also mostly modeled with simplified Maxwell's equation for

electric field and Navier Stokes equation (Eqs. (16) and (17)) for fluid flow. However, for simplicity, it is reported to use phase-field formulation to describe LDEP mechanism. In phase field formulation, the air and liquid volume are treated as one fluid domain with varying physical properties (such as density, viscosity, electrical permittivity, and conductivity) across air-liquid interface [189]. The driving force in liquid dielectrophoresis can be calculated from Eq. (19). However, for dielectric liquid, $\rho_e = 0$ due to an absence of free charge in the liquid and first term on force expression in Eq. (19) can be neglected.

8.2.1 LDEP as pumping mechanism

Pan et al. [190] demonstrated DI water pumping in a microchannel for various channel configurations using LDEP. In their experiment, DI water (as pumped liquid) was surrounded by silicon oil (as a low dielectric medium), and the mixture is placed between plates as shown in Fig. 22A, where the top plate contains blank electrode and bottom plate contains patterned electrodes. The path of water flow is defined by the patterned electrode, which is covered with a dielectric coating. Spacers of different depth were placed on the bottom glass slides to hold liquid of different depth depending on the experimental conditions. The DEP force that drives the liquid depends not only on the applied electric potential, but also on the width of patterned electrodes and depth of flow stream [191]. Figure 22C shows the water stream flowing over the bottom electrode and forming a virtual microchannel. Pumping velocity of water flow in the virtual microchannel was measured by observing the advancement of the water meniscus. The pumping velocity depends on the applied voltage and aspect ratio (d/w) as shown in Fig. 22D. It has been shown that the pumping velocity can be reached as high as 27 mm/s by modulating aspect ratio and applied voltage for 100 kHz AC signal. Their group also demonstrated liquid flowing over wide varieties of electrode designs [190].

Renaudot et al. [192] reported optimization of LDEP devices that can operate as low as 150 V_{rms} between electrodes with 4 μm gap for a liquid having conductivity up to 10 mS/m. LDEP was also used to flow sucrose solution to transport HeLa cell in a microchannel to demonstrate DEP trap and release mechanism [193]. Moreover, LDEP has been reported to use in the transportation of free-floating droplets [195], continuous gas pumping without leaking [195], and liquid actuation on superhydrophobic surfaces [196]. For more information on this micro pumping technique, readers are suggested to consult the detailed review of Kaler et al. [197] and Jones [184].

9 Concluding remarks

Electric field driven pumping mechanisms are popular in microfluidics since they do not require mechanical moving parts, which make them more compatible with micro-total-analytical systems (μTAS) or lab-on-chip format.

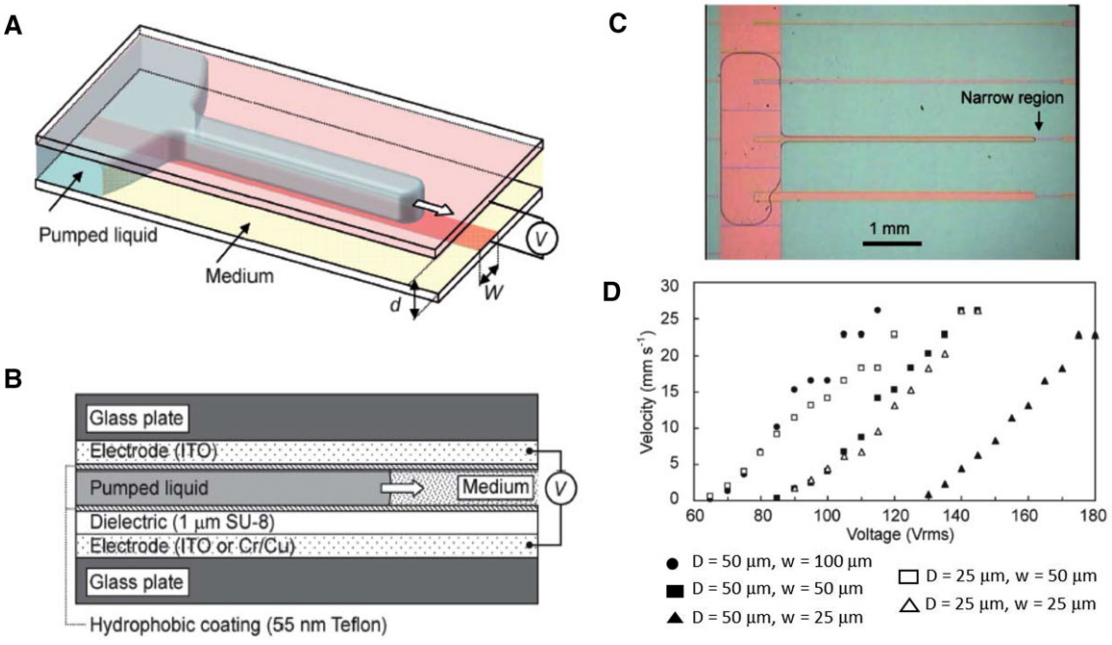

Figure 22. (A) Concept sketching of LDEP pumping mechanism for an electric field defined virtual microchannel. Electric field is applied between unpatterned electrode (top plate) and patterned electrodes (bottom plate) where the channel shape depends on the design of electrode on the bottom plate. (B) Cross-sectional view of device, (C) DI water is flowing over an array of linear electrodes with different width due to the application of 100 kHz AC electric field, and (D) pumping velocity of DI water for various applied electric potentials and aspect ratios i.e. d/w where d is the depth of spacers and w is the width of electrodes. Reproduced from Fan et al. [190] with permission of the Royal Society of Chemistry.

Table 3. General comparisons of selective electric field driven micro pumping mechanisms covered in this review

	Ion drag (EDL formation)			Thermal effect	Particle polarization	
	DCEO or EO	ACEO	ICEO	ACET	twDEP	LDEP
Required conditions for flow in micro/nano-channels	Spontaneous EDL formation due to fixed charge on channel surface	Periodic EDL formation on electrodes due to an applied AC field	Nonuniform EDL formation due to the polarization of metal or neutral post	Nonuniform permittivity and density due to nonuniform temperature as well as space charge	Densely packed micro-particles	Two immiscible fluid media with distinct permittivity
Type of applied electric field	High voltage DC power	Low voltage and low-frequency AC	Intermediate range AC or DC voltage	Low voltage and high-frequency AC	Low voltage AC with phase lag	High AC or DC voltage
Primary driving force	Coulombic forces	Coulombic forces	Coulombic forces	Coulombic and dielectric forces	Dielectric forces and fluid drag	Dielectric forces
Major advantages	Very high pressure and high flow rate, and can be used for pumping	Low electric potential, and can be used for local flow control	Mid range electric potential, and does not create vortices	Low electric potential, and can be used for local flow control with vortices	Suitable for pumping particulate fluids with more controls	Continuous flow of liquids or droplets with high velocity
Primary limitations	Very High voltage is needed, and bubble formation is very common	Negligible pressure build up and undesired flow reversal	Negligible to low-pressure build up	Negligible pressure build up and can only be used to highly conductive buffer	Cannot be used to pump fluids without densely packed particles	Dielectric coating on electrodes are needed, and cannot be used to pump one fluid
Perspective on future research activities	Fundamental research and product development are expected to continue at the current or faster pace	Fundamental research activities are expected to accelerate in near future	Expected to drop due to lack of general interest in this area	Has the potential of significant increase in fundamental research in coming years	Not expected to grow in a significant manner	Failed to generate enough interest and unlikely to make a big splash in future too

DCEO: DC electroosmosis; ACEO: AC electroosmosis; ICEO: induced charge electroosmosis; ACET: AC electrothermal; twDEP: traveling wave dielectrophoresis; LDEP: liquid dielectrophoresis.

This review article provides a systematic description of various electrokinetic phenomena used for micro pumping with detailed physics, unified governing equations, related boundary conditions, and scaling laws. Table 3 shows the comparisons of different electric field driven pumping mechanisms. Depending on the choice of fluid medium, electric field and substrate, one or more phenomena can drive fluids. In some scenarios, one or more phenomena need to be suppressed through design parameters for better control and efficient pumping. Based on the rigorous analysis and literature review presented above, following conclusions can be drawn:

9.1 Electroosmotic pumping

Electroosmosis has been extensively used for pumping in the lab-on-a-chip microfluidic device. Surface coating, channel diameter, and electrode configurations are mainly used to control pumping in DC electroosmosis, while electrode structure and locations are the primary design parameters for AC electroosmosis. Analytical solutions for electroosmotic and mixed electroosmotic-pressure driven velocity distribution are available for DC electroosmotic pumping in rectangular or circular shaped microchannels. For a thin EDL limit, the electroosmotic flow can be modeled with the Helmholtz-Smoluchowski slip velocity at the channel wall. However, deviation from a typical plug-like flow profile can be observed due to non-uniform zeta potential at the channel surface or Joule heating within the channel.

Unlike its DC counterpart, a closed form analytical solution for AC electroosmosis is not possible due to nonlinearity in the electric field. In AC electroosmosis, electrodes are responsible for both creations of the electric field and EDL. Due to the close proximity of the neighboring electrodes, the electric potential applied in AC electroosmosis is much smaller than that of DC. Moreover, in AC electroosmosis, the flow field is highly nonuniform and localized close to the electrode regions. Although AC electroosmosis provides more design parameters, such as electrode geometry and electric field frequency for control, a global flow field cannot be obtained from AC electroosmotic pumping. Depending on the conductivity of the working medium, both DC and AC electroosmotic pumping mechanisms can generate heat as Joule heating [47,198], which can affect the sample in bioseparation process.

9.2 ACET pumping

Like AC electroosmosis, ACET pumping uses coplanar electrode design and AC electric field to create spatially varying heat source to facilitate temperature variation, which is responsible for the ACET flow. However, this mechanism is different from AC electroosmotic pumping in two ways. First, ACET uses much higher electric field frequencies than regular AC electroosmosis. Second, it takes advantage of variable fluid properties to generate spatially varying heat in the system. The complete modeling of ACET involves the solution of the complex electric field, energy, and fluid flow equations. However, the simplified mathematical model based on scaling law analysis can be applied to calculate electric field, which is used to find the dielectric and Coulomb forces. ACET pumping can be controlled by adding an external heating element in addition to modulating the number of energized electrodes and their orientations. ACET can also be supplemented with laser lighting or by including a DC bias to the regular AC electric field. Since the core working principles of ACET involved heat generation, this process might not be suitable for many bioanalyses, where the sample is temperature sensitive. One must carefully evaluate the benefits of using this technique in biological samples if other alternatives are available.

9.3 ICEO pumping

Dipolar double layer, due to the polarization of particles in an electrolyte, is responsible for ICEO. ICEO exhibits non-linear electrokinetics phenomena and becomes dominant physics at the smaller zeta potential. The ICEO can be modeled with Maxwell's equation, Nernst Planck equation, and fluid flow equation where Coulombic force is the driving mechanism for fluid flow. The pumping pressure can vary with applied electric potential as a quadratic relation depending on the frequency, electrolyte, and voltage. ICEO pumping mechanism has some unique advantages over other electroosmotic pumping, such as (i) ICEO pumping can take place in both AC and DC electric field; (ii) the direction of fluid flow and applied electric field directions are perpendicular to each other; and (iii) operational frequency range in ICEO is much wider than the operational frequency range in ACEO.

9.4 DEP pumping

Even though DEP is popularly used for the manipulation of particles, only traveling wave DEP and liquid DEP are used for microfluidic pumping. Travelling wave DEP can be obtained by applying AC electric potential on neighboring electrodes with a 90-degree phase difference. The phase differences on applied electric potential can create a moving electric field in a preferred direction, which can attract or repel particles suspended in fluid resulting in a movement of fluid. Traveling wave DEP can only be applied to a fluid with suspended particles, such as blood. In traveling wave DEP, the direction of the net flow depends on the relative magnitude of traveling wave period and the delay between imposed field and particle moments. If the delay between imposed field and induced particle moment is smaller than the half of the traveling wave period, the fluid flows against the propagating direction and vice-versa. The flow can be modulated through

electrode design, applied electric potential magnitude and frequencies, properties of fluids and particles, etc.

On the other hand, the LDEP is used either to generate a continuous flow of liquid in a liquid-air interface or to move bubbles immersed in a liquid medium. The LDEP pumping mechanism is analogous to the capillary action since it influences hydrostatic equilibrium. This mechanism is different from general electroconvection based electrokinetic pumping. LDEP has been demonstrated to generate flow for both conductive and non-conductive liquid. In LDEP, the pumping velocity depends on the applied electric field, frequencies, the width of the electrode as well as the depth of the flow stream.

The research reported in this publication was supported in part by the National Science Foundation under Grant No. DMS-1317671 and in part by the National Institute of General Medical Sciences of the National Institutes of Health under Award Number R01GM122081. The content is solely the responsibility of the authors and does not necessarily represent the official views of the National Institutes of Health.

The authors have declared no conflict of interest.

10 References

[1] Herr, A. E., Molho, J. I., Drouvalakis, K. A., Mikkelsen, J. C., Utz, P. J., Santiago, J. G., Kenny, T. W., *Analyt. Chem.* 2003, *75*, 1180–1187.

[2] Raisi, F., Belgrader, P., Borkholder, D. A., Herr, A. E., Kintz, G. J., Pourhamadi, F., Taylor, M. T., Northrup, M. A., *Electrophoresis* 2001, *22*, 2291–2295.

[3] Cui, H. C., Horiuchi, K., Dutta, P., Ivory, C. F., *Analyt. Chem.* 2005, *77*, 1303–1309.

[4] Cui, H. C., Horiuchi, K., Dutta, P., Ivory, C. F., *Analyt. Chem.* 2005, *77*, 7878–7886.

[5] Moore, A. W., Jacobson, S. C., Ramsey, J. M., *Analyt. Chem.* 1995, *67*, 4184–4189.

[6] Jacobson, S. C., Hergenroder, R., Koutny, L. B., Ramsey, J. M., *Analyt. Chem.* 1994, *66*, 1114–1118.

[7] Harrison, D. J., Fluri, K., Seiler, K., Fan, Z. H., Effenhauser, C. S., Manz, A., *Science* 1993, *261*, 895–897.

[8] Mosher, R. A., Saville, D. A., Thormann, W., *The Dynamics of Electrophoresis*, VCH, Weinheim, Germany 1992.

[9] Giddings, J. C., *Analyt. Chem.* 1984, *56*, 125–1270.

[10] Gottschlich, N., Jacobson, S. C., Culbertson, C. T., Ramsey, J. M., *Analyt. Chem.* 2001, *73*, 2669–2674.

[11] Hunter, R. J., *Zeta Potential in Colloid Science*, Academic Press, New York, NY 1981.

[12] Reuss, F. F., *Memoires de la Societe Imperiale de Naturalistes de Moscou* 1809, *2*, 327–337.

[13] Wiedemann, G., *Pogg. Ann* 1852, *87*, 321.

[14] Burgreen, D., Nakache, F. R., *J. Phys. Chem.* 1964, *68*, 1084–1088.

[15] Rice, C. L., Whitehead, R., *J. Phys. Chem.* 1965, *69*, 4017–4023.

[16] Kim, M. J., Beskok, A., Kihm, K. D., *Experiments Fluids* 2002, *33*, 170–180.

[17] Dutta, P., Beskok, A., *Analyt. Chem.* 2001, *73*, 5097–5102.

[18] Jian, Y. J., Yang, L. G., Liu, Q. S., *Physics of Fluids* 2010, *22*, 042001.

[19] Luo, W. J., *J. Colloid Interface Sci.* 2004, *278*, 497–507.

[20] Bhattacharyya, S., Nayak, A. K., *Colloids Surf. Physicochem. Engineer. Aspects* 2008, *325*, 152–159.

[21] Liu, Y. P., Jian, Y. J., Liu, Q. S., Li, F. Q., *J. Mol. Liq.* 2015, *211*, 784–791.

[22] Peralta, M., Arcos, J., Mendez, F., Bautista, O., *Fluid Dynamics Res.* 2017, *49*, 035514.

[23] Li, F. Q., Jian, Y. J., Xie, Z. Y., Liu, Y. B., Liu, Q. S., *RSC Advan.* 2017, *7*, 782–790.

[24] Suresh, V., Homsy, G. M., *Physics Fluids* 2004, *16*, 2349–2356.

[25] Ramos, A., Morgan, H., Green, N. G., Castellanos, A., *J. Phys. D* 1998, *31*, 2338–2353.

[26] Lian, M., Islam, N., Wu, J., *Iet Nanobiotechnol.* 2007, *1*, 36–43.

[27] Jubery, T. Z., Srivastava, S. K., Dutta, P., *Electrophoresis* 2014, *35*, 691–713.

[28] Fuhr, G., Schnelle, T., Wagner, B., *J. Micromech. Microengineer* 1994, *4*, 217–226.

[29] Hagedorn, R., Fuhr, G., Müller, T., Gimsa, J., *Electrophoresis* 1992, *13*, 49–54.

[30] Bazant, M. Z., Squires, T. M., *Phys. Rev. Lett.* 2004, *92*, 066101.

[31] Probstein, R. F., *Physicochemical Hydrodynamics: An Introduction*, John Wiley & Sons, Hoboken, NJ 2003.

[32] Kilic, M. S., Bazant, M. Z., Ajdari, A., *Phys. Rev. E* 2007, *75*, 021502.

[33] Squires, T. M., Bazant, M. Z., *J. Fluid Mech.* 2004, *509*, 217–252.

[34] Shim, J., Dutta, P., Ivory, C. F., *Electrophoresis* 2007, *28*, 572–586.

[35] Castellanos, A., Ramos, A., Gonzalez, A., Green, N. G., Morgan, H., *J. Phys. D* 2003, *36*, 2584–2597.

[36] Hossan, M. R., Dillon, R., Dutta, P., *J. Computat. Phys.* 2014, *270*, 640–659.

[37] Liu, Y., Liu, W. K., Belytschko, T., Patankar, N., To, A. C., Kopacz, A., Chung, J. H., *Internat. J. Num. Meth. Engineer.* 2007, *71*, 379–405.

[38] Yoo, K., Shim, J., Dutta, P., *Biomicrofluidics* 2014, *8*, 064125.

[39] Karniadakis, G. E., Beskok, A., Narayan, A., *Microflows and Nanoflows*, Springer, New York, NY 2005.

[40] Dutta, P., Beskok, A., *Analyt. Chem.* 2001, *73*, 1979–1986.

[41] Lu, Y., Ren, Q. L., Liu, T. T., Leung, S. L., Gau, V., Liao, J. C., Chan, C. L., Wong, P. K., *Internat. J. Heat Mass Transfer* 2016, *98*, 341–349.

[42] Chu, A. K. H., *Physical Review E* 2005, *72*, 066311.

[43] Cecchini, M., Girardo, S., Pisignano, D., Cingolani, R., Beltram, F., *Appl. Phys. Lett.* 2008, *92*, 104103.

[44] Ahmed, D., Mao, X. L., Shi, J. J., Juluri, B. K., Huang, T. J., *Lab on a Chip* 2009, *9*, 2738–2741.

[45] Melcher, J. R., *Field Coupled Surface Waves*, MIT Press, Cambridge, MA 1968.

[46] Stratton, J. A., *Electromagnetic Theory*, John Wiley & Sons, Hoboken, NJ 2007.

[47] Horiuchi, K., Dutta, P., Hossain, A., *J. Engineer. Mathemat.* 2006, *54*, 159–180.

[48] Xuan, X. C., Xu, B., Sinton, D., Li, D. Q., *Lab on a Chip* 2004, *4*, 230–236.

[49] Ross, D., Johnson, T. J., Locascio, L. E., *Analyt. Chem.* 2001, *73*, 2509–2515.

[50] Sinton, D., Xuan, X., Li, D., *Experiments Fluids* 2004, *37*, 872–882.

[51] Dutta, P., Beskok, A., Warburton, T. C., *Num. Heat Transfer Part* 2002, *41*, 131–148.

[52] Herr, A. E., Molho, J. I., Santiago, J. G., Mungal, M. G., Kenny, T. W., Garguilo, M. G., *Analyt. Chem.* 2000, *72*, 1053–1057.

[53] Gao, M., Gui, L., *Advances in Microfluidics-New Applications in Biology, Energy, and Materials Sciences*, InTech, London 2016.

[54] Gan, W.-e., Yang, L., He, Y.-z., Zeng, R.-h., Cervera, M. L., de la Guardia, M., *Talanta* 2000, *51*, 667–675.

[55] Zeng, S., Chen, C.-H., Mikkelsen, J. C., Santiago, J. G., *Sensors Actuators B* 2001, *79*, 107–114.

[56] Yao, S., Huber, D., Mikkelsen, J. C., Santiago, J. G., Proceedings of the International Mechanical Engineering Congress and Exposition, New York 2001.

[57] Zeng, S., Chen, C.-H., Santiago, J. G., Chen, J.-R., Zare, R. N., Tripp, J. A., Svec, F., Fréchet, J. M. J., *Sensors Actuators B* 2002, *82*, 209–212.

[58] Lazar, I. M., Karger, B. L., *Anal Chem* 2002, *74*, 6259–6268.

[59] Chen, C.-H., Santiago, J. G., *J. Microelectromech. Syst.* 2002, *11*, 672–683.

[60] Laser, D. J., Goodson, K. E., Santiago, J. G., Kenny, T. W., Proc. 2002 Solid-State Sensor, Actuator, and Microsystems Workshop (Hilton Head Island, SC) 2002.

[61] Takamura, Y., Onoda, H., Inokuchi, H., Adachi, S., Oki, A., Horiike, Y., *Electrophoresis* 2003, *24*, 185–192.

[62] Yao, S., Hertzog, D. E., Zeng, S., Mikkelsen, J. C., Santiago, J. G., *J. Coll. Interface Sci.* 2003, *268*, 143–153.

[63] Laser, D. J., Myers, A. M., Yao, S., Bell, K. F., Goodson, K. E., Santiago, J. G., Kenny, T. W., TRANSDUCERS, Solid-State Sensors, Actuators and Microsystems, 12th International Conference On, 2003, IEEE 2003, pp. 151–154.

[64] Tripp, J. A., Svec, F., Fréchet, J. M. J., Zeng, S., Mikkelsen, J. C., Santiago, J. G., *Sensors Actuators B* 2004, *99*, 66–73.

[65] Razunguzwa, T. T., Timperman, A. T., *Anal Chem* 2004, *76*, 1336–1341.

[66] Chen, L., Guan, Y., Ma, J., Luo, G., Liu, K., *J. Chromatogr. A* 2005, *1064*, 19–24.

[67] Brask, A., Kutter, J. P., Bruus, H., *Lab Chip* 2005, *5*, 730–738.

[68] Chen, Z., Wang, P., Chang, H. C., *Anal Bioanal Chem* 2005, *382*, 817–824.

[69] Yao, S., Myers, A. M., Posner, J. D., Rose, K. A., Santiago, J. G., *J. Microelectromech. Syst.* 2006, *15*, 717–728.

[70] Wang, P., Chen, Z., Chang, H.-C., *Sensors Actuators B* 2006, *113*, 500–509.

[71] Nie, F.-Q., Macka, M., Barron, L., Connolly, D., Kent, N., Paull, B., *Analyst* 2007, *132*, 417–424.

[72] Nie, F.-Q., Macka, M., Paull, B., *Lab on a Chip* 2007, *7*, 1597–1599.

[73] Miao, J. Y., Xu, Z. L., Zhang, X. Y., Wang, N., Yang, Z. Y., Sheng, P., *Advan. Mater.* 2007, *19*, 4234–4237.

[74] Vajandar, S. K., Xu, D., Markov, D. A., Wikswo, J. P., Hofmeister, W., Li, D., *Nanotechnology* 2007, *18*, 275705.

[75] Seibel, K., Schöler, L., Schäfer, H., Böhm, M., *J. Micromechan. Microengineer.* 2007, *18*, 025008.

[76] Joo, S., Chung, T. D., Kim, H. C., *Sensors Actuators B* 2007, *123*, 1161–1168.

[77] Wallner, J. Z., Nagar, N., Friedrich, C. R., Bergstrom, P. L., *Physica Status Solidi* 2007, *204*, 1327–1331.

[78] Edwards, J. M., Hamblin, M. N., Fuentes, H. V., Peeni, B. A., Lee, M. L., Woolley, A. T., Hawkins, A. R., *Biomicrofluidics* 2007, *1*, 014101.

[79] Chen, Y.-F., Li, M.-C., Hu, Y.-H., Chang, W.-J., Wang, C.-C., *Microfluidics Nanofluidics* 2008, *5*, 235–244.

[80] Borowsky, J. F., Giordano, B. C., Lu, Q., Terray, A., Collins, G. E., *Anal Chem* 2008, *80*, 8287–8292.

[81] Berrouche, Y., Avenas, Y., Schaeffer, C., Wang, P., Chang, H.-C., *J. Fluids Engineer.* 2008, *130*, 081604.

[82] Chen, L., Li, Q., Lee, S., Choo, J., *IEEE Sensors J.* 2008, *8*, 488–494.

[83] Ai, Y., Yalcin, S. E., Gu, D., Baysal, O., Baumgart, H., Qian, S., Beskok, A., *J. Colloid Interface Sci.* 2010, *350*, 465–470.

[84] Shin, W., Lee, J. M., Nagarale, R. K., Shin, S. J., Heller, A., *J Am Chem Soc* 2011, *133*, 2374–2377.

[85] Nagarale, R. K., Heller, A., Shin, W., *J. Electrochem. Soc.* 2011, *159*, P14-P17.

[86] Gu, C., Jia, Z., Zhu, Z., He, C., Wang, W., Morgan, A., Lu, J. J., Liu, S., *Anal Chem* 2012, *84*, 9609–9614.

[87] Cao, Z., Yuan, L., Liu, Y.-F., Yao, S., Yobas, L., *Microfluidics Nanofluidics* 2012, *13*, 279–288.

[88] Luong, D., Sprik, R., *ISRN Geophys.* 2013, *2013*, 496352.

[89] Parashchenko, M. A., Filippov, N. S., Kirienko, V. V., Romanov, S. I., *Optoelectron. Instrument. Data Process.*2014, *50*, 315–322.

[90] Li, X., Liu, S., Liang, J., Miyamoto, K. i., Yoshinobu, T., *Phys. Status Solidi* 2016, *213*, 1500–1504.

[91] Darabi, J., Ohadi, M. M., DeVoe, D., *J. Microelectromechan. Syst.* 2001, *10*, 98–106.

[92] Reichmuth, D. S., Kirby, B. J., *J. Chromatogr. A* 2003, *1013*, 93–101.

[93] Pu, Q., Liu, S., *Analyt. Chim. Acta* 2004, *511*, 105–112.

[94] Paul, P. H., Arnold, D. W., Rakestraw, D. J., *Micro Total Analysis Systems' 98*, Springer Dordrecht 1998, pp. 49–52.

[95] Lazar, I. M., Trisiripisal, P., Sarvaiya, H. A., *Anal Chem* 2006, *78*, 5513–5524.

[96] Chen, A., Lynch, K. B., Wang, X., Lu, J. J., Gu, C., Liu, S., *Anal Chim Acta* 2014, *844*, 90–98.

[97] Buie, C. R., Posner, J. D., Fabian, T., Cha, S.-W., Kim, D., Prinz, F. B., Eaton, J. K., Santiago, J. G., *J. Power Sources* 2006, *161*, 191–202.

[98] Shuhuai, Y., Myers, A. M., Posner, J. D., Rose, K. A., Santiago, J. G., *J. Microelectromechan. Syst.* 2006, *15*, 717–728.

[99] Gupta, A., Denver, H., Hirsa, A. H., Stenken, J. A., Borca-Tasciuc, D.-A., *Applied Physics Letters* 2007, *91*, 094101.

[100] Saumitra, K. V., Dongyan, X., Dmitry, A. M., John, P. W., William, H., Deyu, L., *Nanotechnology* 2007, *18*, 275705.

[101] Wang, X., Cheng, C., Wang, S., Liu, S., *Microfluidics and Nanofluidics* 2009, *6*, 145–162.

[102] Tanaka, N., Kobayashi, H., Ishizuka, N., Minakuchi, H., Nakanishi, K., Hosoya, K., Ikegami, T., *J. Chromatogr. A* 2002, *965*, 35–49.

[103] Hayes, J. D., Malik, A., *Anal Chem* 2000, *72*, 4090–4099.

[104] Zhou, L., Lu, J. J., Gu, C., Liu, S., *Anal Chem* 2014, *86*, 12214–12219.

[105] Gonzalez, A., Ramos, A., Green, N. G., Castellanos, A., Morgan, H., *Physical Review E* 2000, *61*, 4019–4028.

[106] Green, N. G., Ramos, A., Gonzalez, A., Morgan, H., Castellanos, A., *Physical Review E* 2002, *66*, 026305.

[107] Green, N. G., Ramos, A., Gonzalez, A., Morgan, H., Castellanos, A., *Physical Review E* 2000, *61*, 4011–4018.

[108] Yokokawa, R., Manta, Y., Namura, M., Takizawa, Y., Le, N. C. H., Sugiyama, S., *Sensors Actuators B* 2010, *143*, 769–775.

[109] Pittman, J. L., Henry, C. S., Gilman, S. D., *Analyt. Chem.* 2003, *75*, 361–370.

[110] Urbanski, J. P., Levitan, J. A., Burch, D. N., Thorsen, T., Bazant, M. Z., *J. Coll. Interf. Sci.* 2007, *309*, 332–341.

[111] Ajdari, A., *Physical Review E* 2000, *61*, R45.

[112] Mpholo, M., Smith, C., Brown, A., *Sensors Actuators B* 2003, *92*, 262–268.

[113] Brown, A., Smith, C., Rennie, A., *Phys. Rev. E* 2000, *63*, 016305.

[114] Ramos, A., Gonzalez, A., Castellanos, A., Green, N. G., Morgan, H., *Phys. Rev. E* 2003, *67*, 056302.

[115] Olesen, L. H., Bruus, H., Ajdari, A., *Phys. Rev. E* 2006, *73*, 056313.

[116] Garcia-Sanchez, P., Ramos, A., Green, N. G., Morgan, H., *IEEE Transact. Dielectrics Electr. Insulat.*2006, *13*, 670–677.

[117] Storey, B. D., Edwards, L. R., Kilic, M. S., Bazant, M. Z., *Phys. Rev. E* 2008, *77*, 036317.

[118] Huang, C. C., Bazant, M. Z., Thorsen, T., *Lab on a Chip* 2010, *10*, 80–85.

[119] Hossan, M. R., Dillon, R., Roy, A. K., Dutta, P., *J. Coll. Interf. Sci.* 2013, *394*, 619–629.

[120] Chiou, P. Y., Ohta, A. T., Jamshidi, A., Hsu, H. Y., Wu, M. C., *J. Microelectromechan. Syst.* 2008, *17*, 525–531.

[121] Melvin, E. M., Moore, B. R., Gilchrist, K. H., Grego, S., Velev, O. D., *Biomicrofluidics* 2011, *5*, 034113–034117.

[122] Ivanoff, C. S., Swami, N. S., Hottel, T. L., Garcia-Godoy, F., *Electrophoresis* 2013, *34*, 2945–2955.

[123] Zhou, H., White, L. R., Tilton, R. D., *J. Colloid Interface Sci.* 2005, *285*, 179–191.

[124] Rezanoor, M. W., Dutta, P., *Biomicrofluidics* 2016, *10*, 024101.

[125] Chung, C. C., Glawdel, T., Ren, C. L., Chang, H. C., *J. Micromechan. Microengineer.* 2015, *25*, 35003.

[126] Ishida, A., Toki, H., Motosuke, M., Honami, S., *J. Therm. Sci. Technol.* 2012, *7*, 475–486.

[127] Hart, R., Lec, R., Noh, H., *Sensors Actuators B* 2010, *147*, 366–375.

[128] Hilber, W., Weiss, B., Saeed, A., Holly, R., Jakoby, B., *Sensors Actuators A* 2009, *156*, 115–120.

[129] Hwang, H., Park, J. K., *Lab on a Chip* 2009, *9*, 199–206.

[130] Song, Y. J., Chen, P. Y., Chung, M. T., Nidetz, R., Park, Y., Liu, Z. H., McHugh, W., Cornell, T. T., Fu, J. P., Kurabayashi, K., *Nano Lett.* 2017, *17*, 2374–2380.

[131] Han, D., Park, J. K., *Lab on a Chip* 2016, *16*, 1189–1196.

[132] Arefin, M. S., Porter, T. L., *J. Appl. Phys.* 2012, *111*, 054919.

[133] Das, D., Yan, Z., Menon, N. V., Kang, Y., Chan, V., Yang, C., *RSC Advan.* 2015, *5*, 70197–70203.

[134] Sigurdson, M., Wang, D. Z., Meinhart, C. D., *Lab on a Chip* 2005, *5*, 1366–1373.

[135] Wu, J., Lian, M., Yang, K., *Appl. Phys. Lett.* 2007, *90*, 234103.

[136] Koklu, A., Tansel, O., Oksuzoglu, H., Sabuncu, A. C., *Iet Nanobiotechnol.* 2016, *10*, 54–61.

[137] Loire, S., Kauffmann, P., Mezic, I., Meinhart, C. D., *J. Phys. D* 2012, *45*, 185301.

[138] Williams, S. J., *Electrophoresis* 2013, *34*, 1400–1406.

[139] Yuan, Q., Wu, J., *Biomedical Microdevices* 2013, *15*, 125–133.

[140] Williams, S. J., Green, N. G., *Electrophoresis* 2015, *36*, 1681–1689.

[141] Kwon, J. S., Wereley, S. T., *Microfluidics and Nanofluidics* 2015, *19*, 609–619.

[142] Green, N. G., Ramos, A., Gonzalez, A., Castellanos, A., Morgan, H., *Journal of Physics D-Applied Physics* 2000, *33*, L13-L17.

[143] Gonzalez, A., Ramos, A., Morgan, H., Green, N. G., Castellanos, A., *Journal of Fluid Mechanics* 2006, *564*, 415–433.

[144] Ng, W. Y., Ramos, A., Lam, Y. C., Wijaya, I. P. M., Rodriguez, I., *Lab on a Chip* 2011, *11*, 4241–4247.

[145] Jiang, H. Y., Li, S. S., Hou, Z. X., Ren, Y. K., Sun, Y. J., *Acta Physica Sinica* 2011, *60*, 20702.

[146] Vafaie, R. H., Ghavifekr, H. B., Van Lintel, H., Brugger, J., Renaud, P., *Electrophoresis* 2016, *37*, 719–726.

[147] Selmi, M., Gazzah, M. H., Belmabrouk, H., *Langmuir* 2016, *32*, 13305–13312.

[148] Wu, Y. P., Ren, Y. K., Jiang, H. Y., *Electrophoresis* 2017, *38*, 258–269.

[149] Salari, A., Navi, M., Dalton, C., *Biomicrofluidics* 2015, *9*, 014113.

[150] Lang, Q., Wu, Y. S., Ren, Y. K., Tao, Y., Lei, L., Jiang, H. Y., *Acs Applied Materials & Interfaces* 2015, *7*, 26792–26801.

[151] Eckstein, Y., Yossifon, G., Seifert, A., Miloh, T., *Journal of colloid and interface science* 2009, *338*, 243–249.

[152] Zhao, C., Yang, C., *Physical Review E* 2011, *83*, 066304.

[153] Pascall, A. J., Squires, T. M., *Journal of Fluid Mechanics* 2011, *684*, 163–191.

[154] Dukhin, S., *Advances in Colloid and Interface Science* 1993, *44*, 1–134.

[155] Mishchuk, N., Takhistov, P., *Colloids and Surfaces A: Physicochemical and Engineering Aspects* 1995, *95*, 119–131.

[156] Lastochkin, D., Zhou, R., Wang, P., Ben, Y., Chang, H.-C., *Journal of Applied Physics* 2004, *96*, 1730–1733.

[157] Gangwal, S., Cayre, O. J., Bazant, M. Z., Velev, O. D., *Physical review letters* 2008, *100*, 058302.

[158] Gregersen, M. M., Okkels, F., Bazant, M. Z., Bruus, H., *New Journal of Physics* 2009, *11*, 075019.

[159] Squires, T. M., Bazant, M. Z., *Journal of Fluid Mechanics* 2006, *560*, 65–101.

[160] Sharp, K., Yazdi, S., Davison, S., *Microfluidics and Nanofluidics* 2011, *10*, 1257–1267.

[161] Sugioka, H., *Physical Review E* 2011, *83*, 056321.

[162] Paustian, J. S., Pascall, A. J., Wilson, N. M., Squires, T. M., *Lab on a Chip* 2014, *14*, 3300–3312.

[163] Feng, H., Huang, Y., Wong, T. N., Duan, F., *Soft Matter* 2017, *13*, 4864–4870.

[164] Bazant, M. Z., Urbanski, J. P., Levitan, J. A., Subramanian, K., Kilic, M. S., Jones, A., Thorsen, T., Proceedings of 11th international conference on miniaturized systems for chemistry and life sciences (MicroTAS) 2007, pp. 2875–2878.

[165] Nobari, M., Movahed, S., Nourian, V., Kazemi, S., *Journal of Electrostatics* 2016, *83*, 97–107.

[166] Canpolat, C., Zhang, M., Rosen, W., Qian, S., Beskok, A., *Journal of Fluids Engineering* 2013, *135*, 021103.

[167] Pohl, H. A., Pohl, H., *Dielectrophoresis: The Behavior of Neutral Matter in Nonuniform Electric Fields*, Cambridge university press, Cambridge 1978.

[168] Sato, M., Yabe, A., Taketani, T., Proceedings of the 1991 ASME JSME thermal engineering joint conference 1991.

[169] Marczak, M., Diesinger, H., *Journal of Applied Physics* 2009, *105*, 124511.

[170] Griffiths, D. J., *AAPT* 2005.

[171] Wang, X., Wang, X.-B., Gascoyne, P. R., *Journal of electrostatics* 1997, *39*, 277–295.

[172] Wang, X.-B., Huang, Y., Becker, F., Gascoyne, P., *Journal of Physics D: Applied Physics* 1994, *27*, 1571–1574.

[173] Huang, Y., Holzel, R., Pethig, R., Wang, X.-B., *Physics in medicine and biology* 1992, *37*, 1499–1517.

[174] Pethig, R., Talary, M. S., Lee, R. S., *IEEE engineering in medicine and biology magazine* 2003, *22*, 43–50.

[175] Tseng, Y.-L., Huang, C.-W., Lei, U., Lin, C.-W., Jaw, F.-S., *Measurement* 2011, *44*, 1980–1985.

[176] Wang, C., Wang, X., Jiang, Z., *Biotechnology & Biotechnological Equipment* 2011, *25*, 2405–2411.

[177] Lei, U., Huang, C., Chen, J., Yang, C., Lo, Y., Wo, A., Chen, C., Fung, T., *Lab on a Chip* 2009, *9*, 1349–1356.

[178] Hughes, M. P., Pethig, R., Wang, X.-B., *Journal of Physics D: Applied Physics* 1996, *29*, 474.

[179] Iverson, B. D., Cremaschi, L., Garimella, S. V., *Microfluidics and nanofluidics* 2009, *6*, 221–230.

[180] He, G., Liu, D., *International Journal of Microscale and Nanoscale Thermal and Fluid Transport Phenomena* 2013, *4*, 5.

[181] Cimpeanu, R., Papageorgiou, D. T., *Phil. Trans. R. Soc. A* 2014, *372*, 20140066.

[182] Wu, Y., Ren, Y., Tao, Y., Jiang, H., *Microfluidics and Nanofluidics* 2017, *21*, 38.

[183] Dong, L., Garimella, S., *Birck and NCN Publications* 2009, *359*.

[184] Jones, T., *Journal of Electrostatics* 2001, *51*, 290–299.

[185] Fax, R., Hurwitz, M., Melcher, J., *Journal of Spacecraft and Rockets* 1969, *6*, 961–967.

[186] Jones, T. B., *Langmuir* 2002, *18*, 4437–4443.

[187] Landau, L. D., Bell, J., Kearsley, M., Pitaevskii, L., Lifshitz, E., Sykes, J., *Electrodynamics of Continuous Media*, Elsevier 2013.

[188] Pellat, H., *C. R. Seances Acad. Sci.* 1894, *675*.

[189] Tian, H., Shao, J., Ding, Y., Li, X., Liu, H., *Langmuir* 2013, *29*, 4703–4714.

[190] Fan, S.-K., Chen, W.-J., Lin, T.-H., Wang, T.-T., Lin, Y.-C., *Lab on a Chip* 2009, *9*, 1590–1595.

[191] Fan, S.-K., Huang, P.-W., Wang, T.-T., Peng, Y.-H., *Lab on a chip* 2008, *8*, 1325–1331.

[192] Renaudot, R., Daunay, B., Kumemura, M., Agache, V., Jalabert, L., Collard, D., Fujita, H., *Sensors and Actuators B: Chemical* 2013, *177*, 620–626.

[193] Chen, N.-C., Chen, C.-H., Chen, M.-K., Jang, L.-S., Wang, M.-H., *Sensors and Actuators B: Chemical* 2014, *190*, 570–577.

[194] Velev, O. D., Prevo, B. G., Bhatt, K. H., *Nature* 2003, *426*, 515–516.

[195] Jiao, J., Almeida, R., Kwon, J. W., *Journal of Microelectromechanical Systems* 2016, *25*, 884–889.

[196] Prakash, R., Papageorgiou, D. P., Papathanasiou, A. G., Kaler, K. V., *Sensors and Actuators B: Chemical* 2013, *182*, 351–361.

[197] Kaler, K. V., Prakash, R., Chugh, D., *Biomicrofluidics* 2010, *4*, 022805.

[198] Horiuchi, K., Dutta, P., *International Journal of Heat and Mass Transfer* 2004, *47*, 3085–3095.

